UM 462, a local green pea galaxy analogue under the MUSE magnifying glass

Monreal Ibero, A.; Weilbacher, P.M.; Micheva, G.; Kollatschny, W.; Maseda, M.

A&A 674, A210 (2023)
https://doi.org/10.1051/0004-6361/202345891

Astronomy & Astrophysics

UM 462, a local green pea galaxy analogue under the MUSE magnifying glass*

Ana Monreal-Ibero[1], Peter M. Weilbacher[2], Genoveva Micheva[2], Wolfram Kollatschny[3], and Michael Maseda[4]

[1] Leiden Observatory, Leiden University, PO Box 9513, 2300 RA Leiden, The Netherlands
e-mail: monreal@strw.leidenuniv.nl
[2] Leibniz-Institute for Astrophysics Potsdam (AIP), An der Sternwarte 16, 14482 Potsdam, Germany
[3] Institut für Astrophysik und Geophysik, Universität Göttingen, Friedrich-Hund Platz 1, 37077 Göttingen, Germany
[4] Department of Astronomy, University of Wisconsin-Madison, 475 N. Charter St., Madison, WI 53706, USA

Received 11 January 2023 / Accepted 3 May 2023

ABSTRACT

Context. Stellar feedback in high-redshift galaxies plays an important, if not dominant, role in the re-ionisation epoch of the Universe. Because of their extreme star formation (SF), the relatively closer green pea (GP) galaxies are postulated as favorite local laboratories, and analogues to those high-redshift galaxies. However, at their typical redshift of $z \sim 0.2$, the most intimate interaction between stars and the surrounding interstellar medium cannot be disentangled. Detailed studies of blue compact dwarf (BCD) galaxies sharing properties with GP galaxies are necessary to anchor our investigations on them.
Aims. We want to study in detail UM 462, which is a BCD with emission line ratios and equivalent widths, stellar mass, and metallicity similar to those observed in GP galaxies, and thus it is ideally suited as a corner stone and reference galaxy.
Methods. We use high-quality optical integral field spectroscopy data obtained with MUSE on the ESO Very Large Telescope.
Results. The electron density (n_e) and temperature (T_e) were mapped. Median T_e decreases according to the sequence [S III] → [N II] → He I. Furthermore, T_e([S III]) values are ∼13 000 K, and uniform within the uncertainties over an area of ∼20″ × 8″ (∼1.4 kpc × 0.6 kpc). The total oxygen abundance by means of the direct method is $12 + \log(O/H) \sim 8.02$ and homogenous all over the galaxy within the uncertainties, which is in stark contrast with the metallicities derived from several strong line methods. This result calls for a systematic study to identify the best strategy to determine reliable metallicities at any location within a galaxy. The strong line ratios used in the BPT diagrams and other ratios tracing the ionisation structure were mapped. They are compatible with plasma ionised by massive hot stars. However, there is a systematic excess in the [O I]/Hα ratio, suggesting an additional mechanism or a complex relative configuration of gas and stars. The velocity field for the ionised gas presents receding velocities in the east and approaching velocities in the west and south-west with velocity differences of $\Delta v \sim 40\,\mathrm{km\,s^{-1}}$, but it is not compatible with simple rotation. The most striking feature is a velocity stratification in the area towards the north with redder velocities in the high ionisation lines and bluer velocities in the low ionisation lines. This is the only area with velocity dispersions clearly above the MUSE instrumental width, and it is surrounded by two ∼1 kpc-long structures nicknamed 'the horns'. We interpret the observational evidence in that area as a fragmented super-bubble fruit of the stellar feedback and it may constitute a preferred channel through which Lyman continuum photons from the youngest generation of stars can escape. The galaxy luminosity is dominated by a young (i.e. ∼6 Myr) stellar population that contributes only 10% to the stellar mass, as derived from the modelling of the stellar continuum. The most recent SF seems to propagate from the outer to the inner parts of the galaxy, and then from east to west. We identified a supernova remnant and Wolf-Rayet stars – as traced by the red bump – that support this picture. The direction of the propagation implies the presence of younger Wolf-Rayet stars at the maximum in Hα. These may be detected by deep observations of the blue bump (not covered here).
Conclusions. The ensemble of results exemplifies the potential of 2D detailed spectroscopic studies of dwarf star-forming galaxies at high spatial resolution as a key reference for similar studies on primeval galaxies.

Key words. galaxies: starburst – galaxies: dwarf – galaxies: individual: UM 462 – galaxies: ISM – galaxies: abundances – galaxies: kinematics and dynamics

1. Introduction

The Galaxy Zoo project (Lintott et al. 2008) revealed a group of compact, extremely star-forming galaxies at low redshift ($z \sim 0.2$), named 'green peas' (GPs) due to their point-like appearance and green colours in the Sloan Digital Sky Survey (SDSS) plates. Their greenish aspect is due to extremely strong emission lines in the optical, in particular [O III]λ5007, with equivalent widths (EWs) of typically several hundreds to ∼1000 Å. Their mass is relatively low ($M \sim 10^{8.5}$–$10^{10.0}\,M_\odot$) and they have one of the highest star formation (SF) rates in the local Universe, reaching values of up to $\sim 10\,M_\odot\,\mathrm{yr}^{-1}$ (Cardamone et al. 2009). Amorín et al. (2010) demonstrated that these were low-metallicity galaxies ($\bar{Z} \sim 0.2\,Z_\odot$). Later on, Izotov et al. (2011) showed that the original 80 GPs were part of a more general population extending over a larger redshift range. They identified ∼800 of these such objects in the SDSS and named them luminous compact galaxies.

Because of their characteristics, GP galaxies constitute a group of galaxies similar to high-redshift galaxies. Thus, they can act as nearby (by comparison) laboratories where one can study the role of the SF in environments as extreme as those occurring in the early Universe. This SF crucially influences the subsequent evolution of the host galaxy at different levels, in

* The reduced cube is only available at the CDS via anonymous ftp to cdsarc.cds.unistra.fr (130.79.128.5) or via https://cdsarc.cds.unistra.fr/viz-bin/cat/J/A+A/674/A210

a far from obvious manner. Specifically, massive stars release huge amounts of momentum, energy, ionising photons, and processed material during their short lives (via stellar winds) and early deaths (via supernova explosions), which has an impact in the neighbouring interstellar medium (ISM). Depending on the geometry of the system, this may extend to the whole host galaxy, its circumgalactic medium, or even beyond, creating outflows of processed material that may escape from the galaxy (i.e. superwinds) or fall back as recycled material ready to form new stars (i.e. fountains). This feedback, which is complex by construction (Tumlinson et al. 2017; Sánchez Almeida et al. 2014), regulates further SF in the galaxy and modulates its chemical evolution. In addition, low-mass star-forming galaxies are one of the favorite candidates as sources of the Lyman continuum (LyC) radiation, responsible for the re-ionisation of the Universe after the cosmic 'Dark Ages' (e.g. Duncan & Conselice 2015; Bouwens et al. 2015, 2016). At low redshift, systems with a large escape fraction of ionising flux are scarce (e.g. Borthakur et al. 2014) with Haro 11 being perhaps the most famous example of a local LyC leaker (Bergvall et al. 2006). In contrast, the GP galaxies (or luminous compact galaxies) display a particularly high LyC detection rate (e.g. Izotov et al. 2016, 2021; Flury et al. 2022a,b).

High-dispersion spectroscopy shows that GP galaxies present complex emission line profiles with distinct kinematics components with different physical and chemical properties (e.g. Amorín et al. 2012; Hogarth et al. 2020). Integral field spectroscopy (IFS) observations have also revealed different kinematic components in these systems (e.g. Bosch et al. 2019). They also suggest that some of these galaxies, but not all, may have gone through a minor merger or interaction event. Thus minor mergers are a possible but not the necessary cause of the strong burst of SF (Lofthouse et al. 2017).

The above results suggest that GP galaxies possess a complex internal structure where several mechanisms shaping the further evolution of the galaxy and its milieu may live together. In addition to the heavy SF, these may include metal-poor gas inflows, processed material outflows, and channels of low H I column density through which LyC photons could leak. However, at the typical distances at which GP galaxies are found, the angular scale ($\sim$3 kpc arcsec^{-1}) is not enough to resolve their inner structure and the most intimate interaction between the sites of extreme SF and the surrounding ISM. This is nevertheless very much needed to get an adequate understanding on the impact of this interaction. Spectroscopic studies at higher spatial resolution, allowing for a proper mapping of the physical and chemical properties of the gas and stars, as well as the kinematics, are necessary to put an anchor on our findings on GP galaxies. High-quality IFS observations of nearby systems similar to GP galaxies are thus instrumental for that.

Local GP analogues can be found among nearby blue compact dwarf (BCD) galaxies (see e.g. Kunth & Östlin 2000; Annibali & Tosi 2022; Henkel et al. 2022, for reviews on these galaxies). These are nearby low-metallicity gas-rich galaxies, undergoing an episode of intense SF. They have low ($M_B \gtrsim -18$) total luminosity and typically large ($\sim 10^8$–$10^9\ M_\odot$) amounts of neutral hydrogen (Thuan & Martin 1981). Once it was thought that they could be genuinely young galaxies forming their first generation of stars. However, deep imaging observations have shown that they contain an extended underlying host population (see e.g. Amorín et al. 2009, and references therein). As a consequence of their massive and on-going SF, all of them present spectra with strong emission lines, similar to those of H II regions, many of them with EW(λ5007) comparable to those of GP galaxies. Even, if they may be fainter than original GP galaxies, their proximity allows us to see the inner workings of a GP(-like) galaxy with an unattainable level of detail in the original GP sample.

IFS has been widely used to study nearby BCDs in the last $\sim$15 years (e.g. García-Lorenzo et al. 2008; Bordalo et al. 2009), allowing us, for instance, to map the physical properties and chemical content of the ionised gas in these systems (e.g. Monreal-Ibero et al. 2012; James et al. 2013; Kumari et al. 2017), to identify outflows (e.g. Monreal-Ibero et al. 2010a; Micheva et al. 2019), or to evaluate the content and distribution of massive stars in a relatively exotic evolutive phase, such as the Wolf–Rayet (WR) phase (e.g. Westmoquette et al. 2013; Monreal-Ibero et al. 2017). In view of the characteristics of the IFS-based instruments to date, works so far have mostly focussed on the innermost regions of the galaxy, more specifically the main sites of SF. Thanks to the advent of the Multi-Unit Spectroscopic Explorer (MUSE; Bacon et al. 2010), with a field of view comparable to the angular size of many BCDs, we can now study these archetypical objects with unprecedented detail, in a more comprehensive manner, and paying attention to the phenomena at play beyond these main sites of SF, including its outermost part and the CGM. This allowed the community, for instance, to identify possible channels for Lyman continuum escape in the halo of SBS 0335−52E (Herenz et al. 2017) or highly ionised outflow cones in ESO 338−IG04 (Bik et al. 2015), sometimes reaching scales of $\sim$15 kpc, which is well beyond the size of the galaxy, as in SBS 0335−52E (Herenz et al. 2023). Likewise, spatially resolved line diagnostics together with emission morphology gave hints that more than one ionisation mechanism is exciting the outer regions in Haro 14 (Cairós et al. 2022). Here, we present one step forward in this direction, by analysing MUSE data of one of these prototypical BCDs.

With an EW([O III]λ5007) $\sim$250 Å (Moustakas & Kennicutt 2006), UM 462 constitutes an example of these BCDs with tremendous EWs, similar to GP galaxies. Its basic characteristics are compiled in Table 1. From the morphological point of view, this low-metallicity galaxy was classified as *iE* by Cairós et al. (2001), meaning that it displays a complex inner structure with several star-forming regions superposed on an external regular envelope. While the galaxy looks pretty compact (effective radius, $r_{e,B} \sim 0.5$ kpc, Amorín et al. 2009), it actually presents a very low surface brightness structure that extends up to $\sim$8 kpc in the north-south direction and up to $\sim$4 kpc in the east-west direction, for the adopted distance here (Micheva et al. 2013). Spectroscopically, this galaxy has been classified as a WR galaxy, with the detection of the so-called blue bump in its spectrum (Izotov & Thuan 1998). This classification has been disputed by James et al. (2010), who did not detect WR features in the integrated spectrum of the galaxy.

Telles & Terlevich (1995) suggested that, together with UM 461 at a projected distance of $\sim$17′ ($\sim$70 kpc at the assumed distance), they form an interacting pair of galaxies. However, this was not supported by later radio observations (van Zee et al. 1998). Besides, even if some kind of interaction with UM 461 occurred, the estimated crossing time (700 Myr) was well longer than the age estimated for the starburst. Another possible cause of the massive SF could be a merger event. Mezcua et al. (2014) show that UM 462 contains two nuclei separated by $\lesssim$600 pc, and that the host galaxy can be fitted well by two components, suggestive of being in the coalescence stage of a (major) merger.

So far, UM 462 has been the subject of two studies based on IFS data. Nicholls et al. (2014) used the spectra of the two

Table 1. Basic data for UM 462.

Parameter	Value	Ref.
Name	UM 462	(a)
Other designations	UGC 06850; Mrk 1307; SDSS 115237−022806	(a)
RA (J2000.0)	11h52m37.2s	(a)
Dec (J2000.0)	−02d28m09.9s	(a)
z	0.003527	(b)
D (Mpc)	14.4	(b)
Scale (pc/″)	70	(b)
$E(B-V)_{\rm Gal}$	0.017	(c)
Morphology	Irr	(d)
c(Hβ)	0.19±0.04	(b)
12 + log(O/H)	$8.03\pm^{0.04}_{0.07}$	(b)
$Z/Z_\odot$	∼0.22 $^{(*)}$	(b)
log(N/O)	$-1.85\pm^{0.14}_{0.15}$	(b)
M_B	−16.36	(e)
$g-r$	0.08	(e)
$M_{\rm HI}$ ($M_\odot$)	3.3×10^8	(e)
$M_\star$ ($M_\odot$)	2.1×10^8	(e)
SFR ($M_\odot$ yr^{-1})	0.11	(e)
$U-B$	−0.66 ± 0.15	(f)
$B-V$	0.36 ± 0.05	(f)
$V-R$	0.08 ± 0.25	(f)
$V-I$	0.07 ± 0.19	(f)
$V-K$	1.77 ± 0.07	(f)
$H-K$	0.39 ± 0.07	(f)

Notes. $^{(*)}$We assumed 12 + log(O/H)$_\odot$ = 8.69 (Asplund et al. 2021).
References. $^{(a)}$NASA/IPAC Extragalactic Database (NED). $^{(b)}$James et al. (2010). $^{(c)}$Schlafly & Finkbeiner (2011). $^{(d)}$Ann et al. (2015). $^{(e)}$Paudel et al. (2018). $^{(f)}$Micheva et al. (2013).

main sites of SF (together with the spectra of other galaxies) to asses the validity of the strong line methods and the so-called direct method to derive oxygen and nitrogen abundances. In a more dedicated study, James et al. (2010) presented detailed 2D spectroscopic mapping of its central region (∼13″ × 13″). They identified at least four star-bursting regions, where they derived the electron temperature and densities as well as several ionic and total abundances, and presented a highly disturbed velocity field for the ionised gas. None of these spectroscopic studies covered the galaxy beyond the main sites of SF.

Here, we present the analysis of deep optical MUSE data covering the whole main body of the galaxy. The underlying question driving this research is: How would a GP(-like) galaxy look if we could resolve it at scales ≲100 pc? The high quality of this unique dataset allows us to obtain spatially resolved information of the physical (i.e. extinction, electron densities and temperatures, degree of ionisation), and chemical properties (ionic and atomic abundances) as well as kinematics of the ISM well beyond the main site of SF. Likewise, we are able to get a basic overview of the characteristics of the underlying stellar population. All together this allows us to gain insight into the impact of the SF on the host galaxy and beyond.

The paper is organised as follows. Section 2 describes the observations and technical details about the data reduction that led to the creation of the datacube. In Sect. 3, we present the general data processing necessary to extract the required information for the analysis. Section 4 contains our results regarding the extinction structure in the system, the physical and chemical properties, ionisation structure, and kinematics of the ionised gas, as well as an overview of the underlying stellar population. Section 5 includes a discussion on the validity of different strong line methods to derive metallicities locally within a galaxy, the presence of specific stellar populations, namely, a possible supernova remnant (SNR) and WR stars, and a discussion on the origin of the ionised gas structures observed in the outer part of the galaxy. Finally, Sect. 6 sumarises our main findings.

2. The data

UM 462 was observed with MUSE (Bacon et al. 2010) as a backup target for the Guaranteed Time Observations (GTO) programme on the 17 April 2018, in four 90° rotated exposures of 500 s each, between 02:15 and 03:01 UTC. The wide-field nominal mode of MUSE without AO support (WFM-NOAO-N) was used for the exposures and relevant calibration. An illumination flat-field exposure was taken right before the first exposure. The seeing reported by the DIMM monitor varied between 1.″3 and 2.″2. The sky conditions were clear without any clouds reported more than 20° above the horizon. The standard star LTT 3218 was observed at the start of the night. Standard daytime calibrations were otherwise used.

The data were reduced with the standard MUSE pipeline (v2.4, Weilbacher et al. 2020), called from within the MuseWise framework (Vriend 2015). Both CCD-level reduction – bias subtraction, flat-fielding, tracing, wavelength calibration, and geometric calibration, and application of these calibrations to the science data – and processing of on-sky calibrations – twilight skyflats, standard stars, and astrometric calibration – used default parameters. The standard star was used for both computation of the response curve and the telluric correction. We employed the default sky subtraction assuming 40% sky within the science field of view. The four exposures were aligned relative to the first exposure, and combined into a single datacube that is corrected for atmospheric refraction and shifted to barycentric velocity.

The final cube is sampled 0.″2 × 0.″2 × 1.25 Å, has a wavelength range of 4749.79−9349.79 Å, covers approximately 60″ × 60″ and has an image quality $FWHM_R \approx 1.''44$ (∼100 pc, at the distance of UM 462), as judged by a Moffat (1969) fit to an image integrated over the R band. The absolute astrometry was adjusted using two stars in the *Gaia* DR2 catalogue (Lindegren et al. 2018). The relative astrometry is correct to better than 0.″1. Before any further analysis, the final cube was corrected for Galactic extinction (see Table 1) and assuming a total-to-selective extinction ratio $R_V = 3.1$, and the Cardelli et al. (1989) extinction curve.

Here, we analyse a portion of 52.″8 × 63.″2, corresponding to 3.7 kpc × 4.4 kpc. That area is presented in Fig. 1, that contains a reconstructed image of the galaxy in the V band with contours tracing the emission in Hα. The figure displays a complex morphology for both stars and gas in the galaxy. Besides, Fig. 2 heralds in a synthetic manner the complexity inherent to this galaxy and serves as a preview of what we shall present and discuss in this work. The first panel shows how most of the stars are located in a series of partially resolved clusters in the north-east to south-west direction, but the extended stellar population is clearly visible. Besides, it signals changes on its properties within the galaxy, with bluer colours in the centre and more reddish colours in the outer parts. The data recover well the structure presented by Micheva et al. (2013), although here with a more limited spatial resolution. The red circle on the northern part of the galaxy is a foreground star, masked in the study presented here.

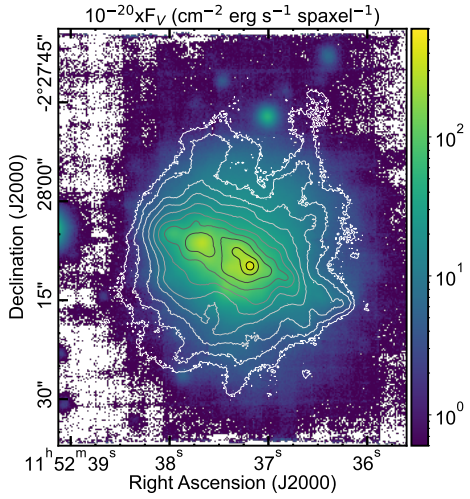

Fig. 1. Reconstructed image of UM 462 made by simulating the action of a broad filter in the V band (see main text for details). A map in Hα flux made by line fitting on a spaxel-by-spaxel basis is overplotted with ten evenly spaced contours (in logarithmic scale) ranging from 1.26×10^{-18} erg cm^{-2} s^{-1} spaxel^{-1} to 1.26×10^{-15} erg cm^{-2} s^{-1} spaxel^{-1}.

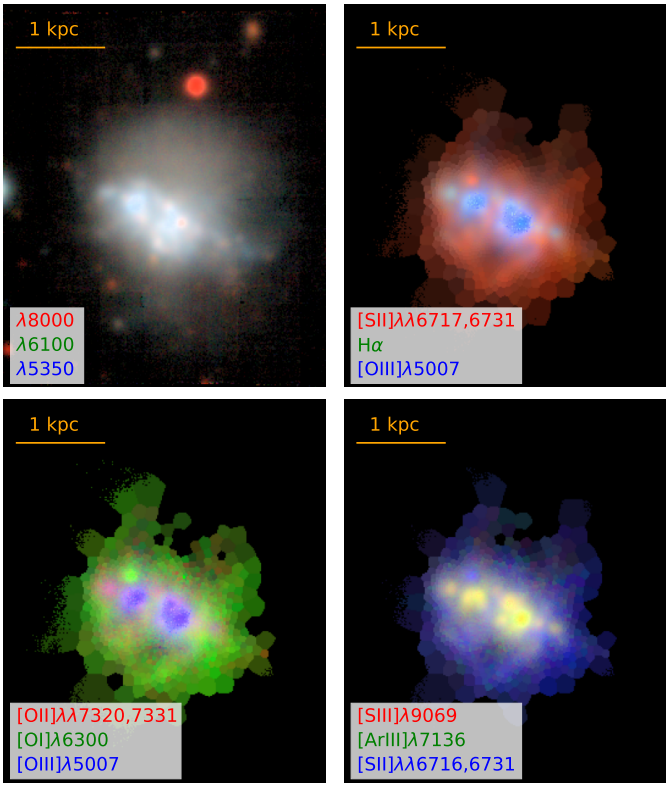

Fig. 2. Set of four RGB images. Individual images were allocated in the corresponding channel ordered by wavelength (i.e. reddest filter in the R channel, central filter in the G channel and bluest filter in the B channel). The *first panel* was made with three images extracted from the MUSE data in 100 Å-wide line-free spectral ranges. Central wavelengths are listed. The other three panels are RGB images made with different sets of emission line fluxes derived by means of Gaussian line fitting, and after having tessellated the MUSE field of view to increase the S/N of the data. The *second panel* contains, together with Hα, two of the strongest CELs, usually used for ionisation parameter mapping (Pellegrini et al. 2012). For the *third panel*, we used emission lines corresponding to three different ionisation degrees for oxygen: neutral, single ionised and two times ionised. The *last one* has maps for lines tracing the two ionisation states available for sulphur, and a line for two times ionised argon, the ion with the highest ionisation potential after the two times ionised oxygen with an available map. All four panels together summarise in a synthetic manner the structural information for the stars and the ionised gas. North is up and east towards the left.

The other three panels illustrate the ionisation stratification within the galaxy, with a dominance of high ionisation lines (e.g. [O III]λ5007) in the centre and of low ionisation lines (e.g. [O I]λ6300) in the outer parts. Subtle differences between these three maps exist, however. The second and third maps were made with lines from ions with relatively different ionisation potential. They present a richer structure with the easternmost and westernmost knots in the central structure of the galaxy having lower ionisation degree than the rest of the central structure (lighter versus darker blue in the second map, pink versus violet in the third map). Besides, there is a bright point-like source towards the north dominated by strong low-ionisation lines (red because of the [S II] lines in the second map, green because of the [O I] line in the third map). These subtleties are much more difficult to identify in the last map since two of ions used here (S^{++} and Ar^{++}) have pretty similar ionisation potential.

3. General post-reduction data processing

We followed two approaches in this study. On the one hand, we did a very detailed spectroscopic analysis of a small subset of regions. On the other hand, we took the most of the 2D spatial information at the expense of sacrificing some diagnostics based on extremely faint spectral features. In order to extract the required information, both of them relied on common post-reduction data processing. This is described here. In the first subsection, we describe how we selected the small subset of regions.

3.1. Definition of the regions and spectral extraction

Ideally, one would like to map as many diagnostic lines as possible to have a complete 2D view of the physical and chemical properties of the gas in the galaxy. For doing so, we applied the Voronoi binning technique (Cappellari & Copin 2003). This algorithm divides the datacube in tiles of different shape and size so that the integrated spectrum within a given tile has always a signal-to-noise ratio (S/N) for a given spectral feature of interest comparable or larger than a given threshold. This guarantees a relatively homogeneous quality of the data. In our particular case, we used the Hα flux map to tesselate the cube, since this traces the morphology of the ionised gas better than any broad band image. We looked for a compromise between having as much spatially resolved information as possible and good detection of the strongest lines, over most of the covered area. The resulting spectra had a mean and median $S/N \sim 8$ in the continuum, measured as the ration between the mean and the standard deviation in 100 Å window centred at 6050 Å. With this tesselation, we recovered maps for the 15 brightest lines, some providing redundant information, like [N II]λ6584 and [N II]λ6548, [O I]λ6300 and [O I]λ6363, or [O III]λ4959 and [O III]λ5007. We used a selection of them to create the three-colour images presented in Fig. 2.

Alternatively, one could extract spectra of larger areas, to obtain as much spectral information as possible at the expense of some lost of spatial information. For doing so, we used the `astrodendro`[1] package that allows us to attach a physical

[1] http://dendrograms.org

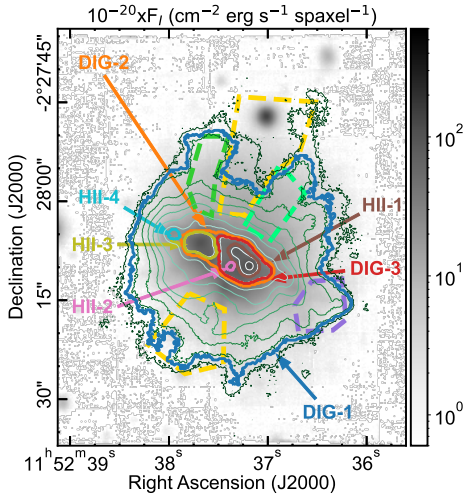

Fig. 3. Reconstructed image of UM 462 made by simulating the action of a broad filter in the I band with contours showing the 'leaves' and 'branches' according to the hierarchical clustering provided by `astrodendro`. Besides, several polygons in dashed lines mark the location of structures within the galaxy of particular interest in terms of ionisation or kinematics. A map in Hα flux made by line fitting on a spaxel-by-spaxel basis is overplotted with ten evenly spaced contours (in logarithmic scale) ranging from 1.26×10^{-18} erg cm^{-2} s^{-1} spaxel^{-1} to 1.26×10^{-15} erg cm^{-2} s^{-1} spaxel^{-1}.

meaning to the extracted regions, at least to a certain extent. This package finds structures in a set of data and groups them hierarchically. The outcome is a set of structures that can be classified as 'leaves', that is to say structures without any sub-structure, and 'branches', i.e. structures with sub-structures within. We use an image in Hα made after fitting the spectrum in each spaxel as input for `astrodendro`. In this way, leaves can be assimilated to the H II regions in the galaxy (up to the spatial resolution of the data), while branches sample areas surrounding the H II regions corresponding to the diffuse component of the ionised gas, at different levels of surface brightness. Given the seeing, we did not apply any Gaussian filtering to the input image, and requested that a given structure should be larger than eight spaxels. In total, we identified four 'leaves' (named H II-i with $i = 1, \ldots, 4$, i increasing from west to east) and three 'branches' (named DIG-i with $i = 1, \ldots, 3$, with i increasing from the outer to the inner parts). The identified regions are displayed in Fig. 3 on top of a reconstructed image in the I band for the galaxy while the corresponding extracted spectra are presented in Fig. 4. There, besides the usual strong emission lines, we see multiple He I lines, at least two iron lines, two faint nitrogen features tracing different ionisation states, [N I]λ5199, and [N II]λ5755. This last line can be used together with [N II]λ6584 to estimate the electron temperature. Besides, the [Cl III]$\lambda\lambda$5518,5538 doublet, useful to estimate the electron density in high-ionisation regions, is also detected. Finally, the blue stellar continuum, as well as some stellar features (most notably Hβ in absorption) are clearly visible.

3.2. Subtracting the emission of the stellar population

The spectrum of (a portion of) a galaxy is made of the added contribution of a stellar (+nebular) continuum, a set of emission lines tracing the ionised gas, and other atomic and molecular absorption features associated to the ISM. To adequately measure the emission line fluxes, these should be separated from their underlying continuum. This is particularly important for features like Hβ, existing both in emission (gas) and absorption (stars). For doing so, we used `FADO`[2] (Gomes & Papaderos 2017). The code reproduces a given observed spectrum by selecting a linear combination of a subset of $N_\star$ spectral components from a pre-defined set of base spectra. Besides, it includes the contribution expected for nebular continuum. Given the low metallicity of UM 462 (see Table 1), this is particularly important here. `FADO` allows the user to adjust certain input parameters, and constrains some of the output parameters, and provides default values for both. In the following, we describe the specific choices that we took that depart from those default values. Regarding the base spectra, we used a selection of single star populations from the set provided by Bruzual & Charlot (2003). These are based on the Padova 2000 evolutionary tracks (Girardi et al. 2000) and assume a Salpeter initial mass function between 0.1 and 100 $M_\odot$. In view of the stellar metallicity already estimated for this galaxy (Micheva et al. 2013) we restricted to those with metallicity $Z = 0.008, 0.004$, making a total of 40 base spectra, with ages ranging from 1 Myr to 15 Gyr. The low stellar mass (see Table 1), also supports our choice of restricting to sub-solar metallicity base spectra. A dwarf galaxy could have high, meaning about solar, metallicity if, for instance, it were the by-product of a major merger of two spiral galaxies, a so-called tidal dwarf galaxy (e.g. Monreal-Ibero et al. 2007; Weilbacher et al. 2003). So far, there is no literature supporting this scenario for UM 462. The spectral range used for the modelling with `FADO` was from 4700 Å to 9275 Å, and included strong stellar features, as Hβ in absorption in the blue and the calcium triplet in the red. We changed the normalisation to 5500 Å, since the value provided by default with `FADO` falls outside of the MUSE spectral range. Besides, key spectral regions containing spectral features not considered by `FADO` (to our knowledge) were masked since they may taint the modelling. In particular, the spectral range from 5770 Å to 5920 Å, was not used since targets with large amount of ISM may display the Diffuse Interstellar Bands at λ5780 and λ5797 (Monreal-Ibero et al. 2018) and/or an excess in the Sodium doublet (Poznanski et al. 2012). The stellar velocity was allowed to vary between -400 km s^{-1} and $+400$ km s^{-1} around the systemic velocity, which was a good compromise between the expected velocity gradients in dwarf galaxies, and leaving room for eventual discovery of high-velocity locations in the galaxy (even if this turned out unnecessary in our case). Finally, we assumed a single extinction law for all the base spectra that was modelled as a uniform dust screen with the extinction law by Cardelli et al. (1989), and allowed for a stellar attenuation up to $A_V\star = 0.9$, since leaving the upper limit as $A_V\star = 6.0$ (the default in `FADO`) predicted unrealistically highly attenuated areas in the outer parts of the galaxy. The best-fit spectra were resampled and subtracted from the original MUSE data. We used these last spectra to measure the emission line parameters, as explained next.

3.3. Line emission measurements

We fitted the different spectral features needed for our analysis by Gaussian functions plus a 1-degree polynomial to take into account local residuals in the continuum substraction using the Python package `LMFIT`[3]. Since we basically followed the same methodology as that throughly described by Monreal-Ibero & Walsh (2020a), we refer to that publication

[2] http://spectralsynthesis.org/fado.html
[3] https://lmfit.github.io/lmfit-py/

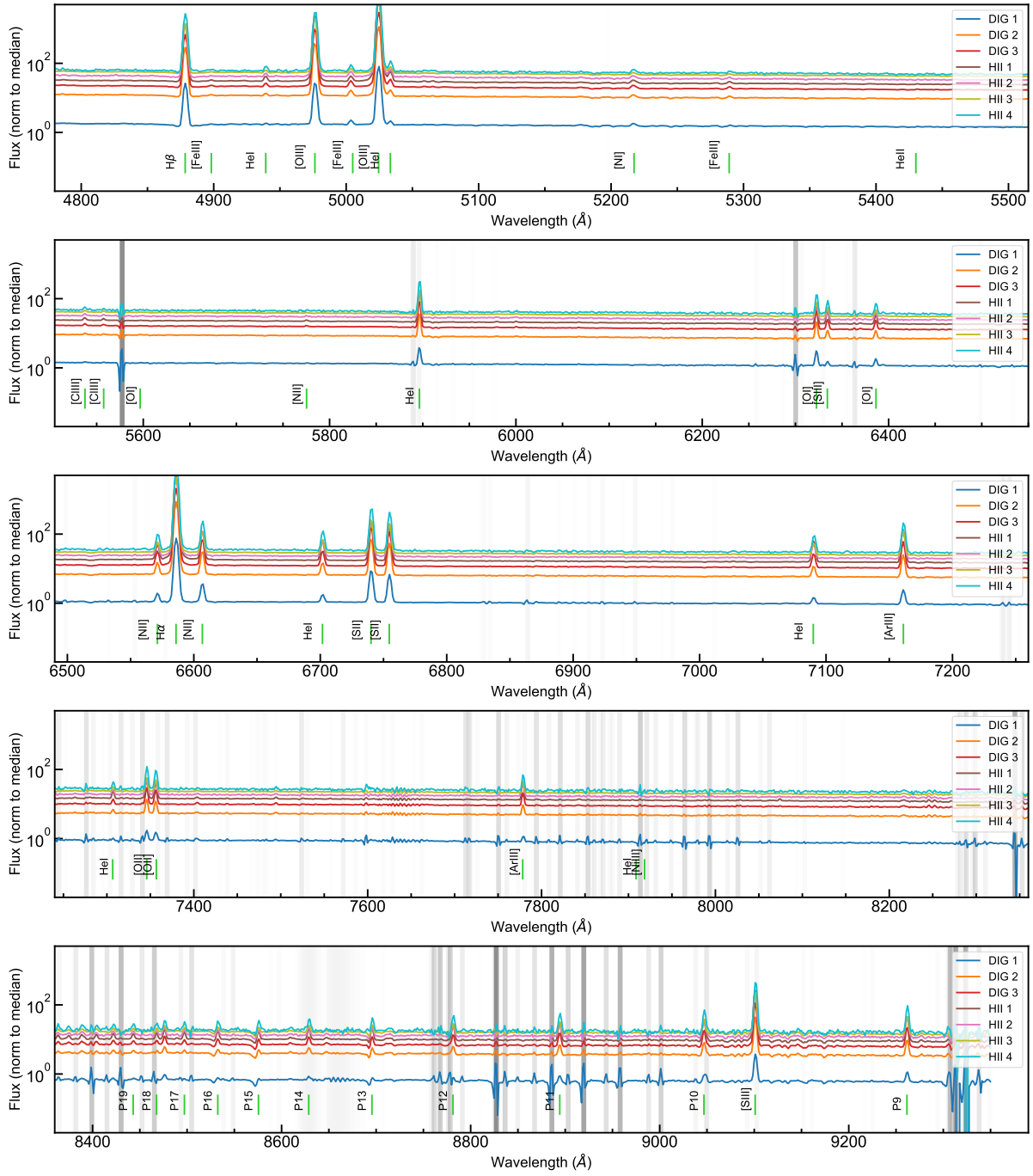

Fig. 4. Integrated spectra for the regions defined by `astrodendro`. Fluxes are presented in logarithmic stretch to optimally visualise at the same time bright and faint features. Spectra have been offset by a factor $\times(1 + 2\,N)$ with N the spectrum number, as indicated by the alphabetically ordering of the labels, to avoid an overlap of the spectra. Small vertical limegreen lines indicate the expected position of the relevant emission lines. The vertical grey bands mark the position of the brightest skylines, the stronger the line is, the more opaque the band appears.

for further details on the line fitting. A set of lines not described in that work is the complex He I$\lambda\lambda$4922,5016 + [O III]$\lambda\lambda$4959,5007 + [Fe III]λ4987. Here, the fitting was rather challenging since there are ∼2 orders of magnitude of difference between the relative fluxes of the [O III] lines and the other lines in the complex. Besides, some of them are strongly blended (e.g. [O III]λ5007+He Iλ5016). Thus, we measure the parameters for the faint lines in the complex only in the selected regions presented in Sect. 3.1. For that we imposed, one and the same line width for the two [O III] lines, and one and the same line width for the other three lines, we fixed the difference in wavelength between the five lines to the expected one according to their rest-frame wavelength and redshift of the galaxy, and we added an offset to the continuum of $\times$1/1000 the peak in [O III]λ5007 (that was taken into account in the fit). A close inspection of this spectral range for the `astrodendro` spectra revealed a broad component at the base of the [O III] lines at the level of $\lesssim$1/500 the peak in [O III]λ5007. These components cannot directly be attributed to the target since they are at a level where the line spread function (LSF) for MUSE is not very well defined. These wings can clearly be seen in other publicly available MUSE data cubes with strong emission lines at high S/N

Table 2. Relative emission line fluxes with respect to $100\times f(\mathrm{H}\beta)$ for summed spectra in the regions defined by `astrodendro`.

Line ID	DIG-1	DIG-2	DIG-3	H II-1	H II-2	H II-3	H II-4
4861 Hβ	100.000±0.157	100.000±0.061	100.000±0.051	100.000±0.037	100.000±0.161	100.000±0.046	100.000±0.170
4922 HeI	0.894±0.014	0.766±0.034	0.825±0.024	1.221±0.027	0.972±0.124	0.891±0.030	1.032±0.114
4959 [OIII]	106.747±0.024	135.933±0.067	150.878±0.048	186.449±0.057	167.988±0.251	158.417±0.060	122.935±0.189
4987 [FeIII]	2.330±0.014	1.901±0.035	1.565±0.024	1.020±0.027	1.554±0.125	1.444±0.031	1.300±0.095
5007 [OIII]	308.500±0.058	392.848±0.173	436.038±0.124	538.836±0.151	485.484±0.658	457.825±0.157	355.283±0.478
5016 HeI	2.187±0.014	2.193±0.036	2.278±0.025	2.839±0.029	2.572±0.131	2.373±0.032	2.456±0.118
5267 [FeIII]	0.868±0.008	0.690±0.014	0.574±0.007	0.393±0.006	0.478±0.034	0.584±0.009	0.392±0.044
5518 [ClIII]	0.249±0.006	0.295±0.010	0.318±0.005	0.328±0.004	0.323±0.025	0.306±0.007	0.380±0.040
5538 [ClIII]	0.191±0.006	0.182±0.010	0.216±0.005	0.222±0.003	0.180±0.024	0.202±0.006	0.154±0.038
5755 [NII]	0.194±0.004	0.130±0.008	0.174±0.004	0.143±0.003	0.171±0.022	0.113±0.005	0.129±0.033
5876 HeI	10.541±0.017	10.295±0.017	10.488±0.021	11.467±0.008	11.243±0.045	10.389±0.013	10.909±0.056
6300 [OI]	8.043±0.013	5.028±0.014	4.679±0.008	3.457±0.011	4.063±0.034	3.431±0.009	3.754±0.042
6312 [SIII]	1.505±0.009	1.730±0.012	1.822±0.007	1.751±0.009	1.986±0.030	1.796±0.008	1.758±0.038
6364 [OI]	2.681±0.006	1.676±0.008	1.560±0.005	1.152±0.006	1.354±0.019	1.144±0.005	1.251±0.024
6548 [NII]	3.483±0.010	2.915±0.019	2.912±0.013	2.344±0.013	2.705±0.056	2.100±0.015	2.372±0.050
6563 Hα	300.000±0.334	299.305±0.145	310.423±0.122	326.461±0.096	317.341±0.415	306.060±0.114	317.428±0.424
6584 [NII]	10.449±0.019	8.746±0.033	8.737±0.023	7.033±0.022	8.115±0.097	6.301±0.026	7.116±0.087
6678 HeI	3.095±0.006	3.009±0.010	3.182±0.005	3.466±0.004	3.296±0.025	3.096±0.007	3.329±0.036
6716 [SII]	32.340±0.037	23.380±0.019	21.420±0.017	15.821±0.009	19.293±0.049	17.185±0.013	19.739±0.056
6731 [SII]	22.694±0.026	16.511±0.017	15.318±0.016	11.684±0.008	13.876±0.044	12.209±0.012	14.072±0.050
7065 HeI	2.221±0.006	2.194±0.009	2.524±0.005	3.676±0.004	2.466±0.024	2.258±0.006	2.379±0.034
7136 [ArIII]	5.952±0.009	6.631±0.011	7.350±0.008	8.511±0.007	8.058±0.033	7.108±0.009	6.822±0.035
7281 HeI	0.460±0.009	0.497±0.008	0.538±0.005	0.647±0.004	0.558±0.021	0.531±0.007	0.574±0.033
7320 [OII]	3.731±0.011	3.230±0.017	3.181±0.011	2.812±0.010	2.885±0.039	2.701±0.013	3.610±0.055
7331 [OII]	3.135±0.012	2.779±0.018	2.688±0.012	2.392±0.010	2.464±0.041	2.289±0.014	3.000±0.059
8752 Pa 12	0.824±0.012	1.107±0.012	1.201±0.006	1.394±0.005	1.297±0.033	1.140±0.009	1.247±0.038
8865 Pa 11	2.338±0.020	1.433±0.010	1.576±0.006	1.782±0.004	1.553±0.026	1.512±0.008	1.643±0.040
9017 Pa 10	2.603±0.014	2.038±0.017	2.112±0.010	2.420±0.007	2.264±0.046	2.039±0.012	2.185±0.061
9069 [SIII]	13.802±0.019	15.269±0.023	17.032±0.015	19.402±0.013	18.839±0.061	16.642±0.018	17.503±0.061
9231 Pa 9	2.773±0.009	2.618±0.014	2.819±0.008	3.226±0.006	2.962±0.036	2.760±0.010	3.066±0.044
$F(\mathrm{H}\beta)$ [(a)]	147.24±26.58	28.90±0.15	66.67±0.58	79.05±0.42	4.62±0.03	44.11±0.21	3.50±0.02

Notes. [(a)]In units of 10^{-15} erg s^{-1} cm^{-2}.

(e.g. Monreal-Ibero & Walsh 2020b) and also in the LSF measured for the sky subtraction during the data reduction. As illustration, Fig. 5 displays those used for slice 20 (top) and 23 (bottom) in all 24 IFUs, in logarithmic stretch. It is clear from the figure that the LSF changes quite a bit on rather small scales (the slices are adjacent on the sky), especially in the wings. Elucidating whether there is information in these broad components beyond the LSF and attributable to the target is a delicate exercise that will not be discussed in this contribution. However it suggests a nice avenue for future research. Finally, derived line widths were corrected by the MUSE LSF for all the lines. This was estimated assuming a Gaussian shape – thus not including the wings mentioned above – and using a polynomial originally derived using the MUSE pipeline and convolved with the 1.25 Å pix^{-1} binning of the cube and had a value of $\sigma \sim 1.18$ Å around [O III]λ5007 and $\sigma \sim 1.06$ Å around Hα.

Fluxes for detected emission lines relative to Hβ in the areas extracted with `astrodendro` are presented in Table 2. They were used to derive the physical and chemical properties presented in Sect. 4.2.

4. Results

4.1. Extinction structure

Extinction for the gas was derived from the Hα and Hβ emission lines and the `RedCorr()` class in `PyNeb`. We assumed an intrinsic Balmer emission line ratio of Hα/Hβ = 2.89 (Osterbrock & Ferland 2006), and the extinction law provided by Cardelli et al. (1989) with $R_V = 3.1$. The derived c(Hβ) map is presented in the upper panel of Fig. 6. Uncertainties, estimated by means of Monte Carlo simulations with 100 realisations, were ∼0.02−0.04. The map is consistent with no extinction over most of the galaxy. The most outstanding exception is an area with a size comparable to that of the seeing disc associated with the peak of emission in Hα, and within H II-1, where c(Hβ) ∼ 0.4−0.5. The extinction map suggests other locations with a more moderate amount of extinction (c(Hβ) ∼ 0.2) coinciding with other secondary peaks of SF (e.g. H II-4 and part of H II-3), unresolved at the spatial resolution of these data. For comparison, James et al. (2010) report c(Hβ) = 0.19 while Nicholls et al. (2014) reports c(Hβ) = 0.128, 0.021 for the two locations analysed in there, roughly corresponding to our H II-1 and H II-3.

Among many other physical quantities, `FADO` also estimates the stellar attenuation needed to reproduce, together with the age and metallicity of the stars, the observed stellar continuum. The corresponding c(Hβ) is presented in the lower panel of Fig. 6. The extinction for the stars is overall smaller than for the gas, as expected.

4.2. The ionised gas

4.2.1. Electron temperatures and densities

Thanks to the high S/N of the extracted spectra, we could derive electron density and temperatures for the seven defined areas based from the extinction corrected fluxes of

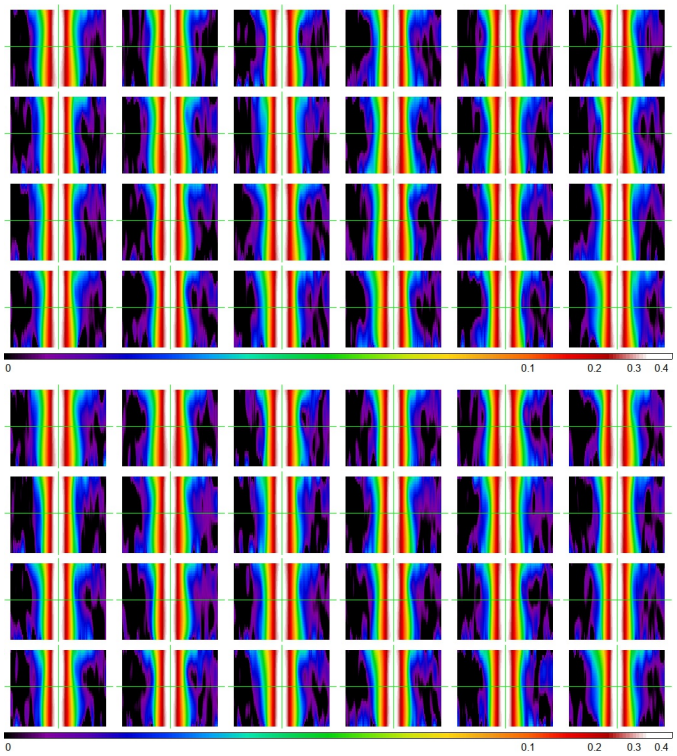

Fig. 5. LSF derived from arc lines for two slices (*top*: slice 20, *bottom*: slice 23) in all 24 MUSE spectrographs. Each of the 24 panels shows the profile for the given slice in one IFU, with the line wavelength increasing vertically from 4650 to 9300 Å. The normalised line profile at each wavelength is distributed horizontally, ±7.5 Å from the line centre.

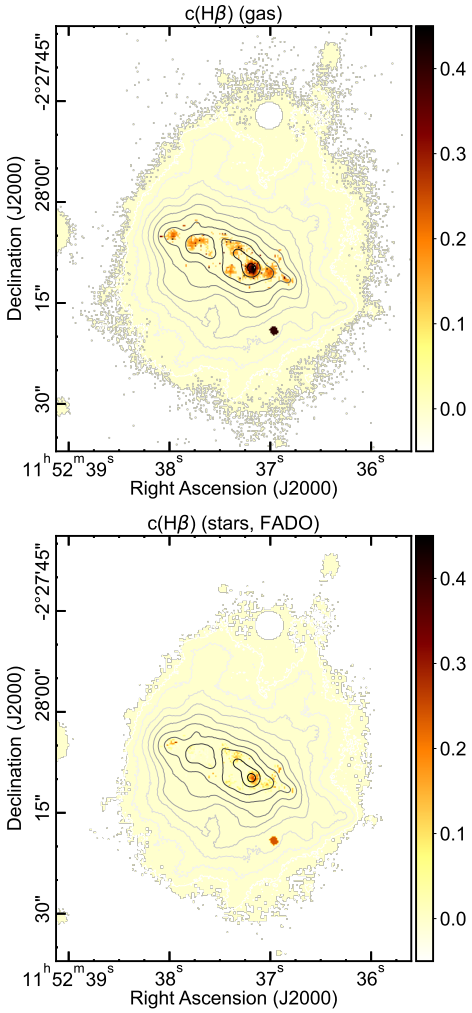

Fig. 6. Mapping the extinction in UM 462. *Top*: log extinction at Hβ, c(Hβ), assuming Hα/Hβ = 2.89, and the Cardelli et al. (1989) extinction law. The median c(Hβ) is 0.04. The estimated median uncertainty for the presented map was ∼0.03, with 90% of the uncertainties ranging between 0.02 and 0.04. *Bottom*: similar information for the stellar populations as derived from FADO.

the collisionally excited lines (CEL) ratios [N II] 5755/6584, [S II] 6731/6716 (lower ionisation plasma), [S III] 6312/9069, and [Cl III] 5538/5518 (higher ionisation plasma). We used the `Atom.getTemDen()` method in the `PyNeb` package (Luridiana et al. 2015), version 1.1.13 with the default set of atomic data (transition probabilities and collision cross sections). We assumed T_e = 12 000 K for the n_e and n_e = 100 cm^{-3} for the T_e. Uncertainties were estimated by means of Monte Carlo simulations with 100 realisations. The reported uncertainties were calculated as half the difference between the 14 and 86 percentile of the distribution of a given outcome of the MC simulation.

Results for the seven selected regions are presented in Table 3. Densities for low ionisation plasma are always in the low density regime. The only exception is H II-1, were they reach values of ∼100 cm^{-3}. Densities for high ionisation plasma seem somewhat higher (∼200 cm^{-3}), although again in the low density regime for that diagnostic. Uncertainties are large for this diagnostic due to the faintness of the chlorine lines.

A widely used description of the thermal structure in a ionised nebula is the three-zone model (Garnett 1992). Here, an ionised area is divided in three zones corresponding to three ranges of ionisation degree. The high-ionisation zone corresponds to ions such as O^{++}, or Ar^{++}, while the intermediate zone to ions such as Ar^{++} or S^{++}, and the low-ionisation zone to species such as O^{+} or N^{+}. The usual approximation is that temperature in each zone is represented by the temperature derived from emission lines of species in that zone. We could estimate the temperatures for the intermediate zone (by means of the [S III] lines) and the low-ionisation zone (by means of the [N II] lines). These, T_e([N II]) and T_e([S III]) are displayed in Fig. 7 with filled circles. Derived T_e([S III]) values are consistent with a uniform temperature of ∼13 000 K all over the galaxy. T_e([N II]) is comparable or systematically lower than T_e([S III]) by up to ∼1200 K. Uncertainties are large, specially in the T_e([N II]) since the flux of the [N II]λ5755 was especially difficult to measure and is subject to large uncertainties but Fig. 7 suggests a relatively homogeneous electron temperature all over the galaxy (i.e. with temperature differences, $\Delta T_e \lesssim$ 1000 K) by means of both diagnostics. We could not measure a diagnostic for the T_e in the high-ionisation zone since the commonly used [O III]λ4363 auroral line is not covered with MUSE. Instead, we used an expression provided by Garnett (1992), that relates T_e([O III]) with T_e([S III]). The derived values in relation with T_e([S III]) are displayed with with stars in Fig. 7). T_e([O III]) are somewhat larger than T_e([S III]) but never beyond 14 000 K. For comparison, Guseva et al. (2007) report a T_e([O III]) = 16 600 K and 13 900 K for two locations in the galaxy that roughly corresponds to our H II 1 + H II 2 and H II 3.

The expressions provided by Garnett (1992) also allow us to put in context our derived T_e([N II]) values. In principle, they should be equivalent to T_e([O II]), since both ions belong to the

Table 3. Physical properties derived from the line fluxes presented in Table 2.

Property	DIG-1	DIG-2	DIG-3	H II-1	H II-2	H II-3	H II-4
$E(B-V)$	$0.01\pm^{0.01}_{0.01}$	$0.02\pm^{0.01}_{0.01}$	$0.06\pm^{0.01}_{0.01}$	$0.12\pm^{0.01}_{0.01}$	$0.10\pm^{0.01}_{0.01}$	$0.06\pm^{0.01}_{0.01}$	$0.10\pm^{0.01}_{0.01}$
n_e([S II]) (cm^{-3})	$50\pm^{60}_{40}$	$70\pm^{80}_{50}$	$70\pm^{120}_{50}$	$110\pm^{110}_{70}$	$60\pm^{10}_{10}$	$70\pm^{80}_{50}$	$40\pm^{10}_{10}$
n_e([Cl III]) (cm^{-3})	$1530\pm^{1480}_{1130}$	$280\pm^{490}_{230}$	$330\pm^{360}_{270}$	$210\pm^{190}_{160}$	$280\pm^{290}_{170}$	$250\pm^{320}_{180}$	$500\pm^{140}_{140}$
T_e([N II]) (K)	$12\,550\pm^{1650}_{1500}$	$12\,900\pm^{1000}_{1000}$	$11\,850\pm^{650}_{400}$	$11\,850\pm^{550}_{400}$	$11\,650\pm^{1200}_{950}$	$12\,200\pm^{850}_{900}$	$11\,750\pm^{2200}_{1650}$
T_e([S III]) (K)	$12\,650\pm^{550}_{450}$	$13\,200\pm^{200}_{200}$	$13\,000\pm^{150}_{150}$	$13\,150\pm^{100}_{100}$	$13\,200\pm^{200}_{150}$	$13\,100\pm^{150}_{150}$	$12\,950\pm^{300}_{250}$
T_e(He I) (K)	...	$7650\pm^{700}_{650}$	$7800\pm^{600}_{500}$	$9150\pm^{400}_{350}$	$7800\pm^{900}_{800}$	$7750\pm^{750}_{750}$	$7650\pm^{850}_{800}$
T_e([O III]) [(a)] (K)	$13\,200\pm^{650}_{550}$	$13\,800\pm^{250}_{250}$	$13\,600\pm^{150}_{200}$	$13\,750\pm^{100}_{100}$	$13\,850\pm^{250}_{150}$	$13\,750\pm^{200}_{200}$	$13\,550\pm^{350}_{300}$
T_e([O II]) [(a)] (K)	$12\,250\pm^{450}_{400}$	$12\,650\pm^{200}_{150}$	$12\,550\pm^{100}_{150}$	$12\,650\pm^{50}_{50}$	$12\,700\pm^{150}_{100}$	$12\,600\pm^{150}_{150}$	$12\,450\pm^{250}_{200}$

Notes. [(a)]Using relations provided by Garnett (1992).

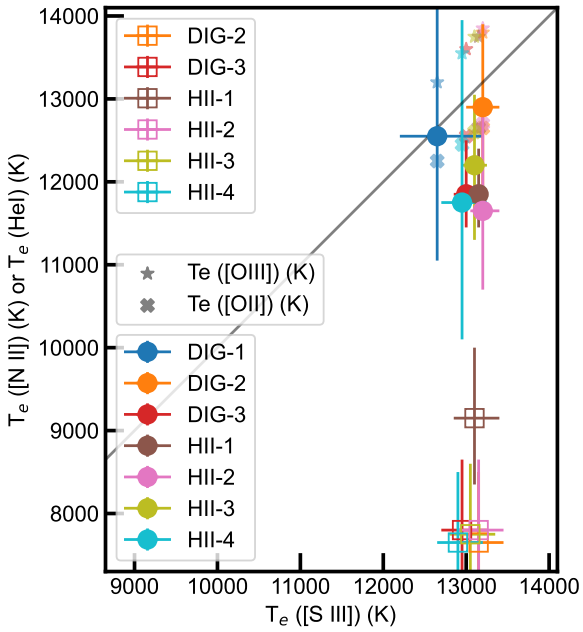

Fig. 7. Comparison of the different derived T_e values. The grey diagonal signals the locus of equal temperatures. Data points with error bars represent our measurements for T_e([N II]) (solid circles) and T_e(He I) (open squares) vs T_e([S III]). Lighter smaller data points without error bars represent the predicted T_e([O III]) (stars) and T_e([O II]) (crosses) as a function of T_e([S III]) according to the relations proposed by Garnett (1992).

same ionisation zone. The crosses in Fig. 7 display T_e([O II]) as derived using those expressions. T_e([N II]) and T_e([O II]) differ by an amount that can range between ~−1000 K and ~300 K. This difference can perfectly be understood simply by taking into account the uncertainty intrinsic to the adopted relation between T_e([O II]) and T_e([S III]), actually a two-step relation, since Garnett (1992) relates T_e([O II]) and T_e([S III]) through T_e([O III]). In a recent paper, Arellano-Córdova & Rodríguez (2020) made a detailed comparison of the different T_e([N II])–T_e([O III]) temperature relation in H II regions published so far, and concluded that, together with the relation provided in their work, the one provided by Garnett (1992) was among the most reliable ones. To our knowledge, there is not a similar work discussing relations involving the T_e([S III]). For the range in temperatures covered here, the uncertainty in the relation for each of the steps would be ~500 K. Considering additional sources of uncertainties, in particular, that associated to the measurement of the flux for the [N II]λ5755 emission line, an absolute difference between the measured T_e([N II]) and derived T_e([O II]) of ~500 K seems reasonable and consistent with both temperatures being in agreement. Anyway, the comparison above stresses the difficulty of deriving reliable temperatures for each ionisation zone in extragalactic (and not particularly distant) objects. For the remaining of the study, when a temperature for a low-ionisation zone was needed, we used T_e([N II]).

The temperature diagnostics discussed so far rely on measurements of CELs. But to prove the physical properties of the optical recombination lines (ORL) emitting regions, line ratios of certain recombination lines can be used. In particular, the He Iλ7281 and He Iλ6678 recombination line ratio constitutes a suitable diagnostic for the ORL temperature (Zhang et al. 2005). We used these lines together with the analytic fits presented by Benjamin et al. (1999) and the most recent emissivities for these lines (Porter et al. 2013) to get an estimation of this temperature, T_e(He I). This ratio does not depend very much on electron density (Zhang et al. 2005). Thus, we simply assumed $n_e = 100$ cm^{-3}. The derived temperatures are in the range of ~7600−9500 K, in all the cases but DIG-1, where we could not derive a reliable T_e(He I). A comparison of these temperatures with T_e([S III]) is presented in Fig. 7 with open squares. T_e(He I) is systematically lower than any CEL-based temperature by a factor ~0.6. As a comparison, López-Sánchez et al. (2007) found in NGC 5253, a BCD galaxy with similar metallicity as UM 462 that T_e(He I) was lower than T_e([S III]) by a factor ~0.8.

Finally, now we shall look to the 2D distribution of the electron density and temperature. The [Cl III] doublet, [N II]λ5755 auroral line, and He Iλ7281 recombination line were too faint to be detected over a substantial area of the galaxy in individual tiles. Thus, we obtained 2D maps for n_e only as derived from the [S II] lines and T_e as derived from the [S III] lines. The electron density map is presented on the left panel of Fig. 8. As suggested by the values derived on selected apertures, UM 462 has values in the low density regime almost everywhere but in the peak of SF, and coincident with the location with the highest reddening. It is already about a decade since pioneer works provided the community with the first n_e density maps in BCDs derived using IFUs (e.g. Monreal-Ibero et al. 2010a, 2012; Telles et al. 2014). In the meantime, the pool of examples has been slowly but steadily increasing. Nowadays, thanks to MUSE, maps covering an important area of the galaxy under study are routinely derived (e.g. Menacho et al. 2021;

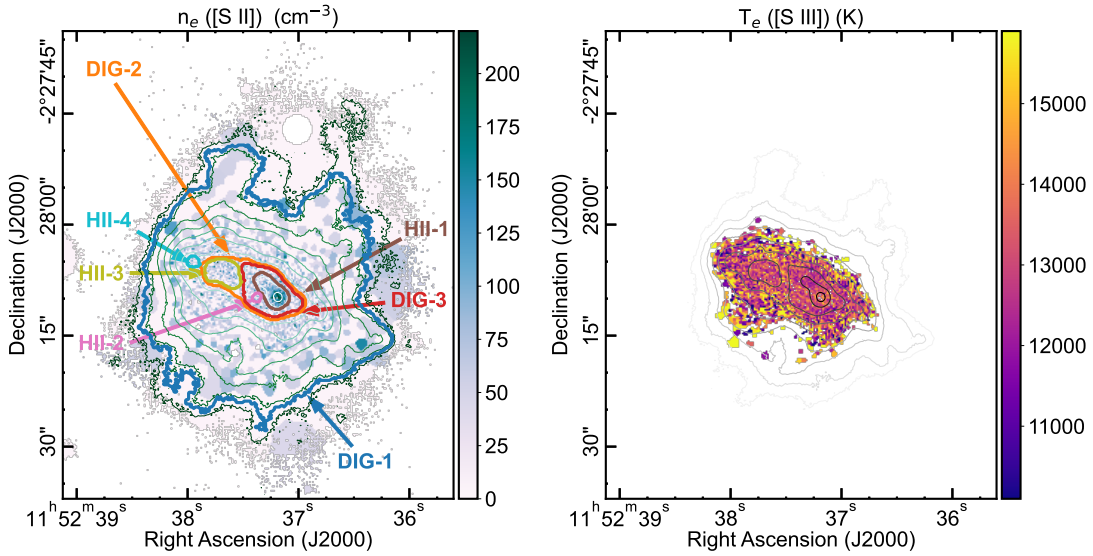

Fig. 8. Mapping the physical properties of the ionised gas in UM 462. *Left*: map of n_e determined from the [S II] emission lines and assuming a $T_e = 12\,000$ K. *Right*: map of T_e determined from the [S III] emission line and assuming a $n_e = 100\,\mathrm{cm}^{-3}$.

Fernández et al. 2023). A recurrent finding in these examples, it is the presence of (more or less) central, and extremely young knots of star formation with larger extinction, and high n_e. These could be interpreted as the observational footprint of star clusters so young that the feedback has not yet not kicked in and the environment around has not yet been fully cleared out.

The electron temperature map is displayed on the right panel. It includes only those spaxels with estimated uncertainties of $\lesssim$2000 K (median ~900 K) and covers an area of ~20″ × 8″ (~1.4 kpc × 0.6 kpc). The 2D electron temperature map does not reveal any particular T_e gradient and simply supports the result for the extracted apertures on the brightest part of the galaxy. This is one of the few T_e maps in BCDs. Monreal-Ibero et al. (2012) discussed maps for T_e([O III]) and T_e([S II]) for NGC 5253, a BCD with metallicity comparable to UM 462, but covering a smaller area (~8″ × 4″ or ~140 pc × 70 pc). T_e([O III]) ranged between 10 000 K and 12 500 K. Besides, Kumari et al. (2018) map T_e([O III]) in a ~3″×5″ (~60 pc × 100 pc) area in NGC 4670. They found values comparable to those found in the inner regions of UM 462. Likewise, Menacho et al. (2021) presented a T_e([S III]) map over an area of ~10 kpc × 10 kpc in Haro 11. As it happens here, T_e was relatively uniform over most of the covered area, with the exception of an area of about ~7 kpc × 3 kpc in the halo with relatively higher temperatures, where fast shocks have been detected.

The measured electron temperatures are comparable to available electron temperature for GP galaxies. For example, Amorín et al. (2012) report T_e([S III]) and T_e([N II]) ~ 12 000−14 000 K for three GP galaxies. This similarity strengthens the role of UM 462 as local GP analogue. Moreover, obtaining spatially resolved information of the electron temperature in GP galaxies is clearly a challenge (because of the faintness of the auroral line). The relative homogeneous T_e([S III]) found here – including the map in Fig. 8 but also the value measured for DIG-1 – supports the idea that a single value representative of the GP galaxy would be enough to characterise a galaxy where such a high spatially resolution as here is not attainable. This would need to be backed up with similar maps from additional GP analogues.

4.2.2. Chemical properties

We derived several ionic and total abundances using the set of lines presented in Table 2. In all the cases, we assumed an n_e([S II]) = 50 cm^{-3} but H II-1, where we used the value reported in Table 3. We did not consider n_e([Cl III]) because of the large uncertainty. Ionic abundances from recombination lines – here only for helium – were calculated using the method `RecAtom.getEmissivity()` in `PyNeb`. Ionic abundances from CELs were determined using the `Atom.getIonAbundance()` method in `PyNeb`. To derive total abundances, we used the `ICF` class. Uncertainties were determined by means of Monte Carlo simulations with 100 realisations, and assuming a normal distribution for the errors of the involved lines. For a given ion, we used as many emission lines as possible to asses the consistency of the results in the apertures defined by `astrodendro`. Besides, for helium, oxygen and nitrogen we derived 2D abundance maps using the strongest lines for their ions. Derived ionic and total abundances as well as used ionisation correction factors (ICFs) for the selected apertures are listed in Table 4. There, rows shaded in grey mark the adopted total abundance for a given element. The reported uncertainties were calculated as half the difference between the 14 and 86 percentile of the distribution of a given outcome of the MC simulation.

Helium. There are several singlet and triplet recombination He^+ lines within the MUSE spectral coverage. Here, we measured fluxes for three singlet (λ4922, λ5016, and λ6678), and two triplet (λ5876, and λ7065) lines. While lines in the singlet cascade are insensitive to radiative transfer effects, these can have an impact in lines belonging to the triplet cascade, and in particular, in λ7065 (see Monreal-Ibero et al. 2013 and references therein for a discussion on these effects). A choice should be made also about the assumed temperature to calculate the helium abundance. Many works in the literature use T_e([O III]). However, in our case, this was not directly measured from our data, but an estimate that relies on other T_e measurements. Abundances reported were derived using T_e([S III]). To assess the robustness of the derived values, we also calculated the helium abundances using the helium emissivities at the measured T_e(He I). Differences were $\lesssim$0.1%, much smaller than the

Table 4. Ionic and total abundances for helium, oxygen, nitrogen, sulphur, argon and chlorine in selected apertures.

Property	DIG 1	DIG 2	DIG 3	H II 1	H II 2	H II 3	H II 4
He^+/H^+ (λ4922)$\times10^2$	7.20±2.27	6.11±2.78	6.10±3.27	9.15±4.53	7.10±5.78	7.03±3.37	7.93±3.62
He^+/H^+ (λ5016)$\times10^2$	7.29±1.58	6.72±2.18	7.61±2.61	9.30±3.24	8.35±4.14	7.51±2.31	8.08±2.40
He^+/H^+ (λ5876)$\times10^2$	7.80±1.31	7.82±11.47	7.81±1.18	8.13±1.20	8.17±2.01	7.74±1.12	7.85±1.18
He^+/H^+ (λ6678)$\times10^2$	7.95±0.92	7.90±7.71	7.90±0.99	8.17±0.79	8.15±1.35	7.81±1.01	7.96±1.02
He^+/H^+ (λ7065)$\times10^2$	7.95±0.74	7.82±5.39	7.97±1.00	8.34±2.14	8.13±0.94	7.82±0.87	7.91±0.77
$He^+/H^+ \times10^2$	7.86±0.50	7.84±4.25	7.86±0.49	8.18±0.58	8.16±0.74	7.77±0.47	7.89±0.48
O^0/H^+ (λ6300)$\times10^5$	0.67±0.25	0.39±0.11	0.44±0.07	0.32±0.04	0.40±0.11	0.36±0.11	0.40±0.26
O^0/H^+ (λ6364)$\times10^5$	0.67±0.28	0.40±0.10	0.49±0.07	0.32±0.03	0.46±0.14	0.38±0.11	0.36±0.17
O^+/H^+ (λ7320)$\times10^5$	3.56±2.17	3.02±1.17	4.47±1.05	3.16±0.63	4.15±2.14	3.90±1.65	4.92±2.93
O^+/H^+ (λ7331)$\times10^5$	4.12±3.14	3.12±1.12	4.32±1.03	3.40±0.76	4.19±1.57	3.99±1.25	5.16±4.49
O^{++}/H^+ (λ4959)$\times10^5$	5.25±0.69	6.21±0.26	6.97±0.22	8.39±0.19	7.26±0.25	7.14±0.20	5.80±0.33
O^{++}/H^+ (λ5007)$\times10^5$	5.16±0.61	5.97±0.22	6.81±0.22	8.11±0.18	7.02±0.25	6.84±0.23	5.57±0.31
$O/H\times10^5$	9.18±2.44	9.57±0.98	11.92±0.84	11.72±0.61	11.25±1.48	10.50±0.90	11.99±6.96
$12+\log(O/H)$	$7.96\pm^{0.10}_{0.13}$	$7.98\pm^{0.04}_{0.05}$	$8.08\pm^{0.03}_{0.03}$	$8.07\pm^{0.02}_{0.02}$	$8.05\pm^{0.05}_{0.06}$	$8.02\pm^{0.04}_{0.04}$	$8.08\pm^{0.20}_{0.38}$
N^0/H^+ (λ5199)$\times10^6$	0.35±0.16	0.22±0.05	0.27±0.04	0.18±0.02	0.26±0.08	0.18±0.04	0.19±0.10
N^+/H^+ (λ6584)$\times10^6$	1.15±0.26	0.96±0.17	1.09±0.11	0.85±0.09	1.05±0.20	0.83±0.16	0.88±0.35
$ICF(N)_{I06}$ [a]	2.06±1.05	2.83±1.05	2.34±0.44	3.22±0.56	2.45±1.65	2.46±1.08	1.96±1.08
$N/H\times10^6_{I06}$ [a]	1.49±0.42	1.17±0.22	1.36±0.16	1.03±0.11	1.32±0.28	1.01±0.21	1.07±0.44
$12+\log(N/H)$ [a]	$6.37\pm^{0.22}_{0.49}$	$6.43\pm^{0.20}_{0.37}$	$6.39\pm^{0.12}_{0.17}$	$6.44\pm^{0.10}_{0.13}$	$6.39\pm^{0.26}_{0.72}$	$6.29\pm^{0.21}_{0.44}$	$6.24\pm^{0.32}_{1.15}$
$\log(N/O)$ [a]	$-1.48\pm^{0.27}_{0.83}$	$-1.51\pm^{0.16}_{0.25}$	$-1.68\pm^{0.09}_{0.11}$	$-1.66\pm^{0.08}_{0.10}$	$-1.67\pm^{0.17}_{0.28}$	$-1.67\pm^{0.12}_{0.17}$	$-1.97\pm^{0.34}_{0.40}$
S^+/H^+ (λ6716)$\times10^6$	0.79±0.15	0.49±0.08	0.54±0.06	0.38±0.04	0.52±0.09	0.41±0.05	0.57±0.20
S^+/H^+ (λ6731)$\times10^6$	0.75±0.19	0.49±0.11	0.51±0.06	0.37±0.04	0.52±0.10	0.41±0.07	0.55±0.18
S^{++}/H^+ (λ9069)$\times10^6$	1.25±0.11	1.32±0.04	1.40±0.03	1.40±0.02	1.40±0.03	1.36±0.03	1.35±0.04
S^{++}/H^+ (λ6312)$\times10^6$	1.31±0.25	1.32±0.07	1.41±0.05	1.38±0.05	1.41±0.07	1.35±0.05	1.35±0.10
$ICF(S)_{I06}$ [a]	1.06±0.04	1.08±0.04	1.06±0.02	1.09±0.03	1.08±0.07	1.07±0.04	1.05±0.08
$S/H\times10^6_{I06}$ [a]	2.17±0.55	1.95±0.22	2.03±0.15	1.94±0.11	2.09±0.34	1.90±0.16	2.04±0.60
$12+\log(S/H)$	$6.34\pm^{0.10}_{0.13}$	$6.29\pm^{0.05}_{0.05}$	$6.31\pm^{0.03}_{0.03}$	$6.29\pm^{0.02}_{0.02}$	$6.32\pm^{0.07}_{0.08}$	$6.28\pm^{0.03}_{0.04}$	$6.31\pm^{0.11}_{0.15}$
$\log(S/O)$	$-1.61\pm^{0.13}_{0.19}$	$-1.69\pm^{0.07}_{0.08}$	$-1.76\pm^{0.04}_{0.05}$	$-1.77\pm^{0.04}_{0.04}$	$-1.73\pm^{0.07}_{0.09}$	$-1.73\pm^{0.05}_{0.06}$	$-1.77\pm^{0.23}_{0.49}$
Ar^{++}/H^+ (λ7136)$\times10^7$	2.77±0.25	2.90±0.09	3.16±0.07	3.35±0.07	3.23±0.07	3.03±0.07	2.85±0.09
$ICF(Ar)_{I06}$ [a]	1.08±0.02	1.08±0.03	1.07±0.00	1.08±0.01	1.08±0.04	1.08±0.02	1.08±0.04
$Ar/H\times10^7_{I06}$ [a]	3.01±0.55	3.14±0.22	3.41±0.16	3.63±0.15	3.51±0.21	3.27±0.17	3.09±0.26
$12+\log(Ar/H)$	$5.48\pm^{0.07}_{0.09}$	$5.50\pm^{0.03}_{0.03}$	$5.53\pm^{0.02}_{0.02}$	$5.56\pm^{0.02}_{0.02}$	$5.54\pm^{0.03}_{0.03}$	$5.51\pm^{0.02}_{0.02}$	$5.49\pm^{0.04}_{0.04}$
$\log(Ar/O)$	$-2.48\pm^{0.14}_{0.20}$	$-2.48\pm^{0.05}_{0.06}$	$-2.54\pm^{0.04}_{0.04}$	$-2.50\pm^{0.03}_{0.03}$	$-2.51\pm^{0.06}_{0.07}$	$-2.50\pm^{0.04}_{0.05}$	$-2.58\pm^{0.20}_{0.39}$
Cl^{++}/H^+ (λ5518)$\times10^8$	1.33±0.37	1.46±0.15	1.56±0.10	1.55±0.05	1.55±0.16	1.52±0.11	1.77±0.29
Cl^{++}/H^+ (λ5538)$\times10^8$	1.35±0.50	1.22±0.21	1.48±0.12	1.46±0.07	1.15±0.22	1.40±0.14	1.06±0.40
$ICF(Cl)_{I06}$ [a]	1.27±0.04	1.27±0.05	1.27±0.01	1.28±0.03	1.27±0.03	1.27±0.02	1.31±0.11
$Cl/H\times10^8_{I06}$ [a]	1.70±0.96	1.71±0.33	1.93±0.18	1.93±0.13	1.72±0.35	1.86±0.26	1.93±0.71
$12+\log(Cl/H)$	$4.23\pm^{0.19}_{0.36}$	$4.23\pm^{0.08}_{0.09}$	$4.29\pm^{0.04}_{0.04}$	$4.29\pm^{0.03}_{0.03}$	$4.24\pm^{0.08}_{0.10}$	$4.27\pm^{0.06}_{0.07}$	$4.29\pm^{0.14}_{0.20}$
$\log(Cl/O)$	$-3.73\pm^{0.20}_{0.39}$	$-3.74\pm^{0.09}_{0.12}$	$-3.79\pm^{0.06}_{0.06}$	$-3.78\pm^{0.04}_{0.04}$	$-3.82\pm^{0.09}_{0.12}$	$-3.75\pm^{0.07}_{0.09}$	$-3.78\pm^{0.37}_{0.43}$

Notes. [a]ICFs in Eqs. (18)b, and (20)b, (21)b, and (22)b by Izotov et al. (2006).

estimated uncertainty. We used the ratio between the λ6678 and λ7065 lines to evaluate the relative importance of radiative transfer effects. We found these basically non-existent in every aperture but in H II-1 which were negligible ($\tau(\lambda3889) \sim 0.020$, for a ratio between radial and thermal velocity of $\omega \sim 3$). This is within the expectation given the derived low electron density.

Abundances by means of the different helium lines are reported in Table 4. For a given aperture, all the lines give consistent results. Since the measurement of the fluxes for the faint and (and heavily blended) lines λ4922 and λ5016 were of considerably lower quality, we used the abundances derived from lines λ5876:λ6678:λ7065, with a weight 3:1:1 to derive the single ionised helium abundance. We also derived a 2D map of He^+/H^+, this time only using the strongest line (see Fig. 9). He^+/H^+ is the highest at H II-1 and the lowest in DIG-1, suggesting a larger contribution of neutral helium when going towards the outer parts

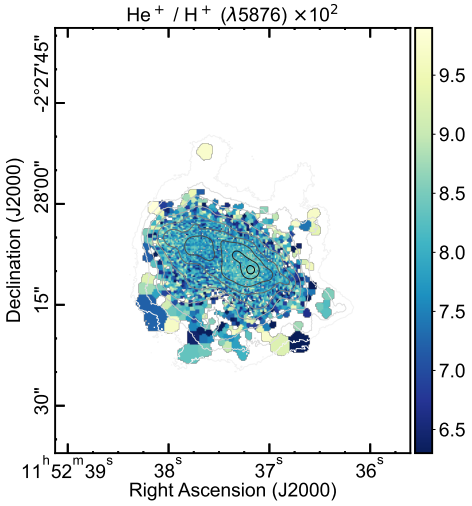

Fig. 9. Map for the He^+/H^+ abundance derived from the He Iλ5876 emission line. North is up and east towards the left.

of the galaxy. As for comparison, James et al. (2010) report an $He/H = 8.73 \pm 0.72 \times 10^{-2}$. This is comparable within the uncertainties but somewhat higher with the values measured here.

Regarding He^{++}, MUSE in normal mode do not cover the strongest optical line (He IIλ4686), and we did not detect the much fainter He II line at λ5411 in any or our apertures. James et al. (2010) report that, if He II were present, then it presents an abundance $\lesssim$1/50th that of He I. Thus, we consider its contribution here as to be negligible.

Oxygen. The MUSE spectral range covers optical lines tracing neutral, singly ionised and doubly ionised oxygen. For this last ion, we used both the [O III]λ4959 and [O III]λ5007 lines together with the values derived for T_e([O III]). For singly ionised and neutral oxygen, we adopted a temperature of $T_e = 12\,100$ K, the average of the T_e([N II]) values. Regarding singly ionised oxygen, the [O II]λ7320 and [O II]λ7331 lines (actually, four lines seen as a doublet at the MUSE spectral resolution) may be affected by a certain O^{++} recombination contribution. Following the correction scheme proposed by Liu et al. (2000), we estimated a negligible contribution here. Finally, neutral oxygen abundance was derived using the [O I]λ6300 and [O I]λ6363 lines. Total abundances were calculated by addition of ionic abundances. For the selected apertures, the two [O II] lines were equally weighted, and the two [O III] lines were weighted 3:1, as the two [O I] lines. Results for the selected apertures are presented in Sect. 4.2.2, while maps for the ionic and total abundances appear in Fig. 10.

The comparison with the results by James et al. (2010), when possible (our regions H II-1– their regions 1+3, H II-2[+ DIG3] – approximately, their region 2, and H II 3 – approximately, their region 4), shows an agreement within the uncertainties. The relative abundances of neutral, single and double ionised oxygen in the different apertures already delineate the variation in ionisation conditions from higher ionisation degree (in H II-1, where the proportion of O^{++} is the highest and that of O^0 is the lowest) to lower ionisation degree (DIG-1, where the situation is reversed). This is much better seen in the 2D abundance maps (see Fig. 10) where all the ions are presented with the same scale to make the comparison of the relative ionic abundances easier. Regarding total oxygen abundance, within the reported uncertainties, this is uniform all over the galaxy, and indicates a metallicity for the galaxy of $Z \sim 0.25\,Z_\odot$, well within the range of metallicities derived for GP galaxies (Izotov et al. 2011; Amorín et al. 2010).

The direct method is considered the gold standard in terms of determining element abundances in extragalactic astronomy. In that sense, the map presented in Fig. 10 is, probably, among the largest oxygen abundance maps, in terms of covered area, determined by means of this method (see also Menacho et al. 2021 for a similar map in Haro 11). However, given the difficulty to measure the auroral line(s), strong line methods are more routinely used instead. Because of the importance of identifying metallicity gradients or inhomogeneities in dwarf galaxies, we discuss in Sect. 5.1 how the map derived here compares to the results by some of the most widely used strong line methods.

Nitrogen. We used the [N I]λ5199 emission line (actually a blended doublet at the MUSE spectral resolution) to determine the abundance in neutral nitrogen, and the [N II]λ6584 line for the single ionised nitrogen. For both, N^+ and N^0, we employed the T_e([N II]) values. Derived ionic abundances are listed in Table 4. To our knowledge, this is the first time that neutral nitrogen abundances are reported for UM 462. Regarding ionised nitrogen, we find an abundance about $\times$2 larger than those reported by James et al. (2010).

The sum of these two ionic abundances is clearly higher in the areas far from the main sites of star formation (e.g. DIG-1, DIG-2) than in the brightest H II regions (e.g. H II-1). The results of the ionic abundances for oxygen suggests unseen further (i.e. two times or more) ionised nitrogen in the main sites of SF but does not reject an inhomogeneity in nitrogen abundance with lower total nitrogen at those locations. When the abundance of one or several ions of a given element is not available, it is customary the use of different ionisation correction factor (ICF) schemes that rely on the available abundances of ions of other elements with comparable ionisation potentials to those of the ionic species of the element of interest. Here, we adopted those presented by Izotov et al. (2006) for intermediate oxygen abundances, derived using emission-line galaxies observed in the frame of the SDSS. The derived total nitrogen abundance and relative to oxygen abundances are displayed in Table 4. Results using the ICF provided by Torres-Peimbert & Peimbert (1977, not shown) were the same within the uncertainties. The map in Fig. 11 suggests a mild ($\lesssim$0.20 gradient of log(N/O) crossing the galaxy in the north-east to south-west direction (i.e. H II-4 with $\log(N/O) \sim -1.8 \rightarrow$ H II-1 with $\log(N/O) \sim -1.6$). This is of the order of the estimated uncertainty and thus, compatible with an homogeneity in relative nitrogen-to-oxygen abundance within the galaxy. For the metallicity derived here, GP galaxies have a relative nitrogen-to-oxygen abundance of $-1.6 < \log(N/O) \sim -0.9$ (Amorín et al. 2010). The value found for UM 462 puts this galaxy just at the lower limit of the typical nitrogen-to-oxygen abundance measured in GP galaxies.

Sulphur, argon and chlorine. We could derive also ionic and total abundances in the selected apertures for some additional elements with somewhat more uncertain ICFs. They are all presented here.

Regarding sulphur, the MUSE spectral range offers information to derive ionic abundances for S^+ and S^{++}. We used either T_e([N II]) or T_e([S III]), depending on whether we wanted to determine single or double ionised sulphur abundance. As with nitrogen, the sum of these two ionic abundances is lower in the main sites of SF than in the diffuse component of the ionised gas, suggesting the presence of three times ionised sulphur in there. Total abundances using the ICF provided by Izotov et al. (2006) are also listed in Table 4. Values are compatible with a

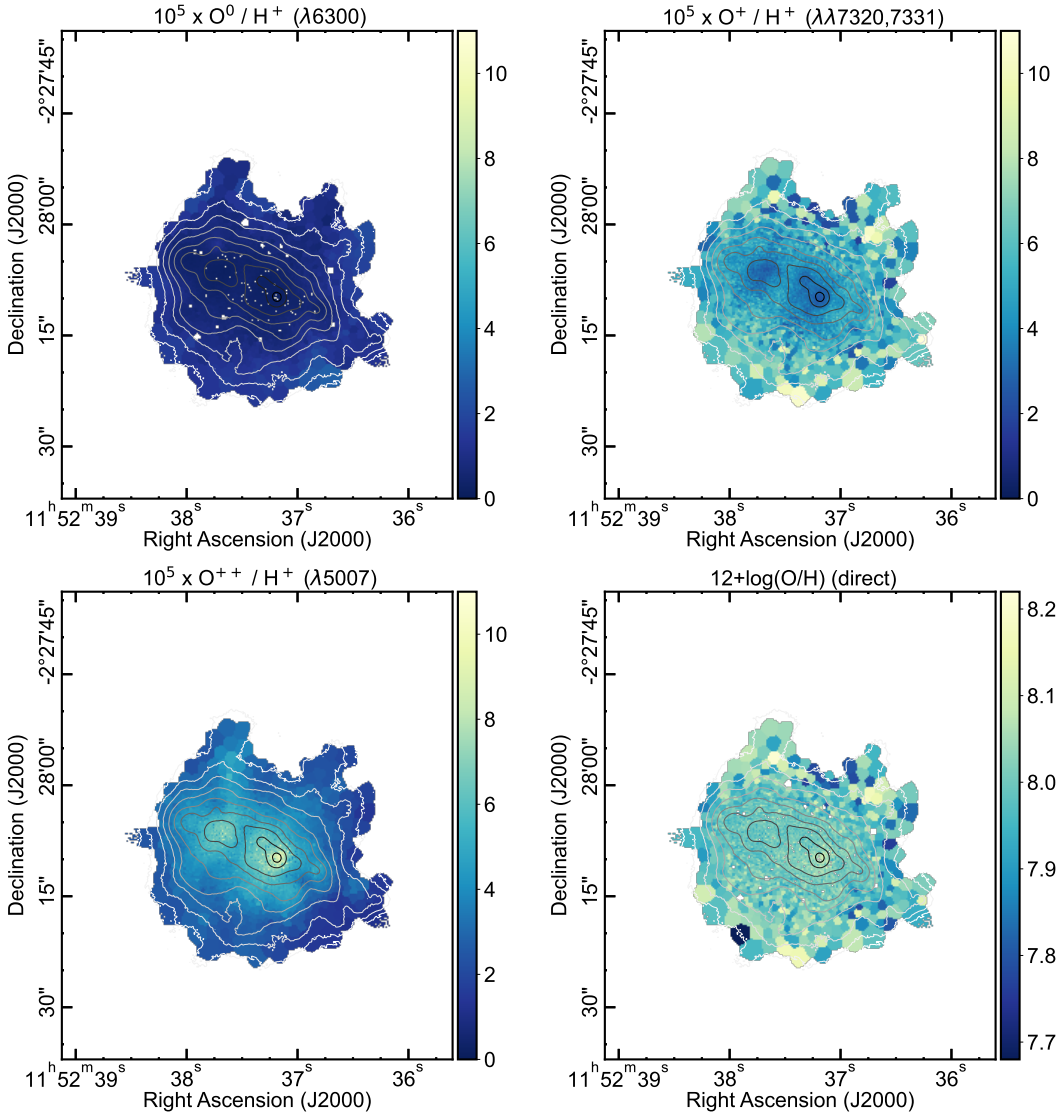

Fig. 10. Maps for the O^{++} (*top left*), O^{+}, (*top right*), and O^{0} (*bottom left*) ionic abundances, derived using the direct method as described in the text. All the three maps display the same range in abundance in order to emphasise the relative contribution of each ion in the different parts of the galaxy. The last map in this figure (*bottom right*) contains the total oxygen abundance map, 12 + log(O/H). North is up and east towards the left.

uniform abundance in sulphur. They are systematically higher than those reported by James et al. (2010), although in some apertures they are compatible within the uncertainties. Differences may be attributed to the different T_e values used in both works.

Finally, we could derive ionic abundances for two times ionised argon and chlorine (Ar^{++} and Cl^{++}). In both cases, we used T_e([S III]). These are both ions with relatively high ionisation potentials (27.63 eV and 23.81 eV, respectively), comparable to that of S^{++} (23.34 eV). As a consequence, higher ionic abundances are seen in the main site of SF, in particular H II-1, than in the rest of apertures under consideration. Again, total abundances were estimated by means of the ICF schemes provided by Izotov et al. (2006) and are consistent with uniform abundance over the galaxy.

4.2.3. Emission line ratio in the BPT diagnostic diagrams

A widely used tool to gain insight into the ionisation mechanisms playing a role in the ISM is the use of diagnostic diagrams, where different areas of a given diagram are occupied by gas excited via different mechanisms. Probably, the most popular ones are those proposed by Baldwin et al. (1981) and later reviewed by Veilleux & Osterbrock (1987): the so called BPT diagrams. In their origin, the different areas in the diagrams were defined using the nuclear or integrated information of a set of astrophysical objects, including H II regions (and starburst galaxies), planetary nebulae, and different types of active galactic nuclei. Then, the different areas in the diagrams were named after the kind of objects that could be found in there, and when information for a new object was obtained, the position in those diagrams was used to identify the main ionisation mechanism at play. Nowadays, the same information is routinely derived for portions (in an ample variety of scales) of astrophysical objects, including anything from a planetary nebulae to high redshift galaxies, and the one-to-one association between the position of a given set of data in the diagram and the original label associated with the objects used to define these diagrams is not so straightforward any more. Ionisation mechanisms not considered originally like shocks (e.g. Monreal-Ibero et al. 2006, 2010b),

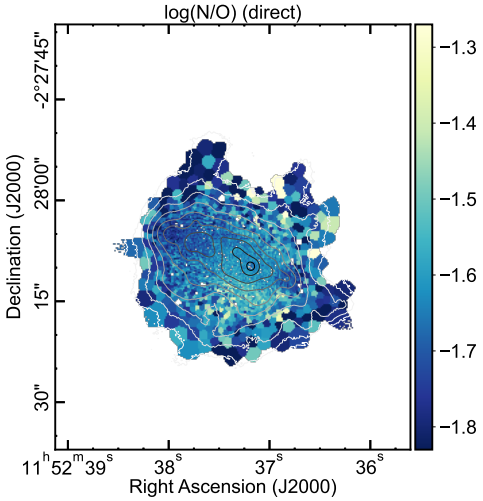

Fig. 11. Map for the relative nitrogen-to-oxygen abundance derived using the direct method as described in the text. North is up and east towards the left.

AGB stars (e.g. Flores-Fajardo et al. 2011; Kehrig et al. 2012; Zhang et al. 2017), or leaking photons from an H II region (e.g. Della Bruna et al. 2021; Weilbacher et al. 2018; Papaderos et al. 2013) produce spectra with line ratios falling in areas in the BPT diagrams that overlap those originally defined. However, as long as one has this in mind, these diagrams are still a useful tool to explore the ionisation structure within, for example, a given galaxy and learn about the causes of the observed line ratios.

Maps for the line ratios involved in the three BPT diagrams are presented in Fig. 12 and the positions of each individual tile in the diagrams themselves are presented in Fig. 13. Clearly, the ionisation structure is quite complex and the joint information of the maps and the diagrams allow us to identify some well defined substructures within the system.

The [N II]/Hα[4] map displays the most regular distribution of the four. Ratios are the lowest in the main sites of SF, in particular H II-1 and H II-3, and increase in a relatively smooth and unstructured manner when going towards the external parts of the galaxy. Overall, [S II]/Hα and [O I]/Hα present a similar distribution as [N II]/Hα (i.e lowest values in H II-1 and H II-3, then increasing outwards). However, both maps are more structured and more closely following the Hα flux maps (contours in all the presented maps). On first order, [O III]/Hβ has a reversed distribution (i.e a structure following the Hα flux maps but with higher values in H II-1 and H II-3, then decreasing outwards). There are further subtle differences between these maps and the one for [N II]/Hα. First, there are two horn-like structures in the northern part of the galaxy, hereafter called 'the horns'. Their borders are marked in Fig. 3 with two green dashed polygons. The eastern one roots at H II-3 and while the western at H II-1. Both extend towards the north for ∼1 kpc. Their typical ratios in the BPT diagrams are represented with green polygons in Fig. 13. Excluding the main sites of SF, they are the locations with the highest [O III]/Hβ line ratios, with somewhat larger ratios in the eastern horn. Both present moderate and basically indistinguishable [S II]/Hα and [O I]/Hα line ratios but eastern one has lower [N II]/Hα ratios by ∼0.15 dex.

The southern half of the galaxy presents at least one structure in Hα, reminiscent of the northern horns (and actually brighter). It roots at the complex H II-1/H II-2/DIG-3, extending towards the south first, then bending towards the east. However, all the southern half is much less structured in terms of line ratios. These simply increase (or decrease for [O III]/Hβ) with distance from the main site of SF. This structure is easier to identify in the equivalent width maps (see Sect. 4.2.6).

There is an additional resolved structure that stands out in the maps: an ear-like region towards the east, hereafter called 'the ear', marked in Fig. 3 with a purple dashed polygon. It has relatively high [S II]/Hα and [O I]/Hα even if not the highest, and covers a relatively large range in [O III]/Hβ, including the lowest values measured within the galaxy. As we shall see in Sect. 4.2.7, it is the region with the bluest velocities in Hα and [O III]λ5007.

Finally, at coordinates RA (J2000) = 11:52:37.8 and Dec (J2000) = −02:28:03.0, there is a local maximum in the [S II]/Hα and [O I]/Hα maps with line ratios barely distinguishable from their surroundings in the [O III]/Hβ line map, and completely undistinguishable in the [N II]/Hα map. This location is unresolved at our seeing, and it does not seem clearly associated with any knot of SF, according to the our continuum images, or the broad band images provided by Micheva et al. (2013), at higher spatial resolution. We discuss the nature of this source in Sect. 5.2.

When looking at the position of each tile in the BPT diagram, the data points mostly fall below the theoretical borders proposed by Kewley et al. (2001), even if in the diagram involving the [O I]/Hα, data points are just at the border. This would suggest that this plasma is primarily photoionised by massive stars. However, this maximum theoretical borders were defined based on models covering up to much larger metallicites than the one of UM 462. Theoretical borders based only on models at the metallicity, $Z = 0.004$ (dotted-dashed lines in Fig. 13), closer to that of UM 462 would be more suitable. These are marked in the diagrams with indigo lines. They were derived using models that take into account the impact of the binary star population, that produces more Wolf-Rayet and hot stars at older ages (Xiao et al. 2018). While data points are clearly consistent with photoionisation by massive stars in the [N II]/Hα and [S II]/Hα diagrams, it seems that the [O I]/Hα diagram requires an additional mechanism (e.g. shocks) or a specific configuration of the relative distribution of gas and stars (e.g. a patchy distribution of the ISM as in the picked-fence scenario Heckman et al. 2001; Bergvall et al. 2006; Ramambason et al. 2020). Either way, this is more important in DIG-1 than in the main sites of SF, specially in the part between the horns which, as we shall see in Sect. 4.2.7, presents high velocity dispersion and different velocities depending on the ionic species.

4.2.4. Emission line ratios mapping the ionisation structure

Beyond the line ratios involved in the BPT diagrams, some additional diagnostics have been proposed in the literature as proves of the ionisation structure. For example, Pellegrini et al. (2012) used maps of the [O III]λ5007/[S II]$\lambda\lambda$6716,6731 line ratio to assess the optical depth of the ionising radiation in individual H II regions. In a way, this is a compact manner of jointly looking at the two axes of the [O III]/Hβ versus [S II]/Hα diagram. Besides, to avoid (or at least minimise) dependencies on elemental abundances, one could use ratios involving lines coming from different ionisation stages of a given element

[4] We use the following nomenclature: [N II]/Hα for [N II]λ6584/Hα, [S II]/Hα for [S II]$\lambda\lambda$6716,6731/Hα, [O I]/Hα for [O I]λ6300/Hα, [O III]/Hβ for [O III]λ5007/Hβ. When other lines are used, these will be explicitly mentioned.

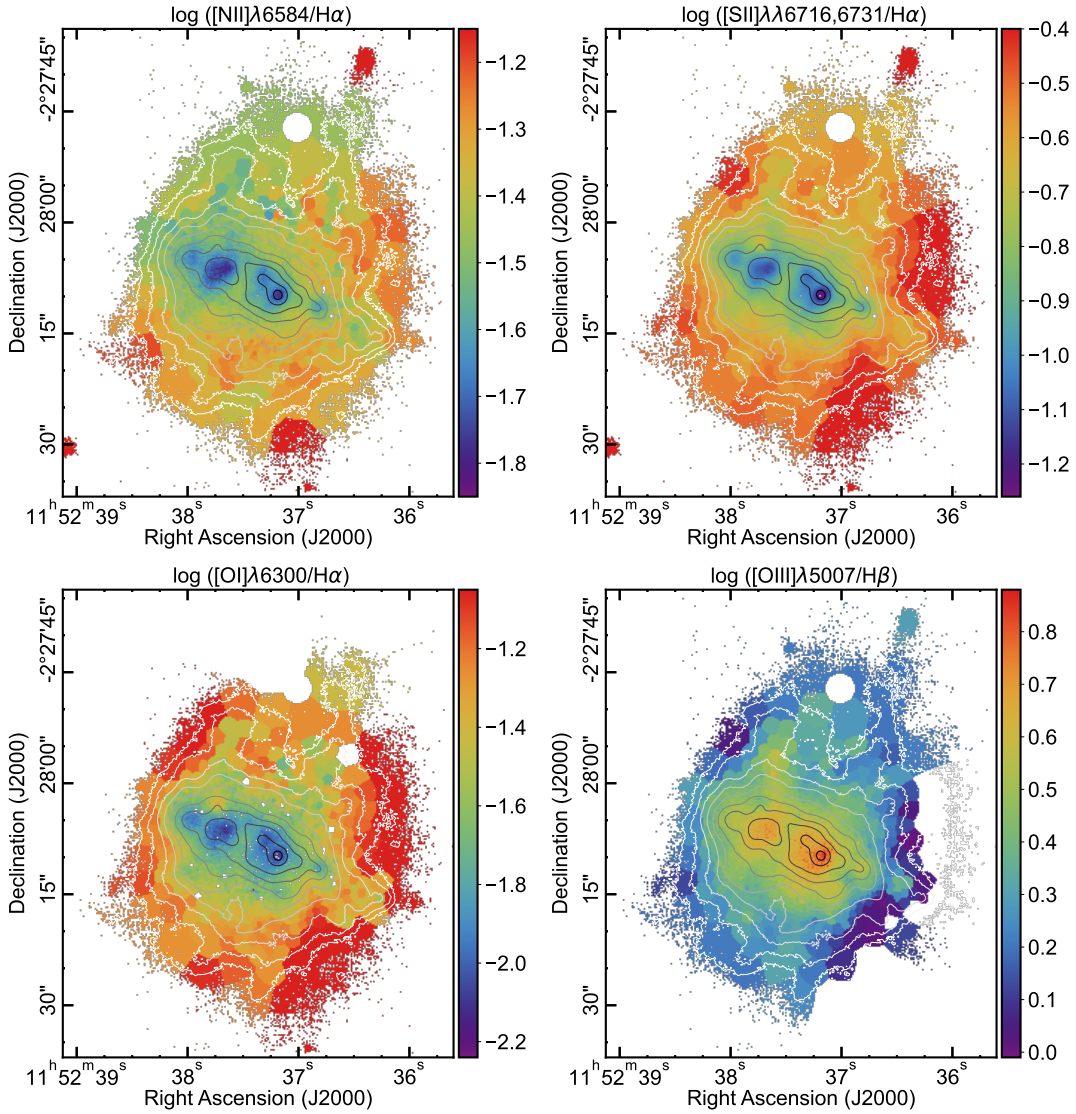

Fig. 12. Maps for the line ratio involved in the so-called BPT diagrams (Baldwin et al. 1981). North is up and east towards the left.

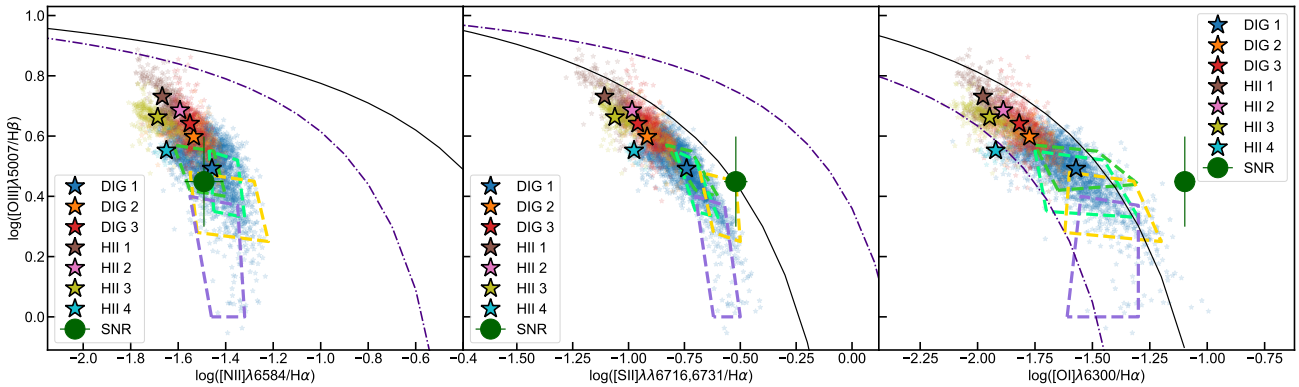

Fig. 13. Position of the individual tiles (small translucent stars) and the regions defined by `astrodendro` (large solid stars) in the so called BPT diagnostic diagrams (Baldwin et al. 1981). Black continuous lines show the theoretical borders proposed by Kewley et al. (2001) to delimit the area where the line ratios can be explained by star formation, while indigo dashed-dotted lines mark the maximal starburst prediction for an object with metallicities $Z = 0.004$, as derived by Xiao et al. (2018). The big green circle in each diagram represents the line ratios for the unresolved source at RA (J2000) = 11:52:37.8 and Dec (J2000) = −02:28:03.0, once fluxes have been decontaminated by the diffuse gas emission of the galaxy. The four irregular polygons with dashed lines aproximately delimit the locii of line ratios measured in the regions marked in Fig. 3.

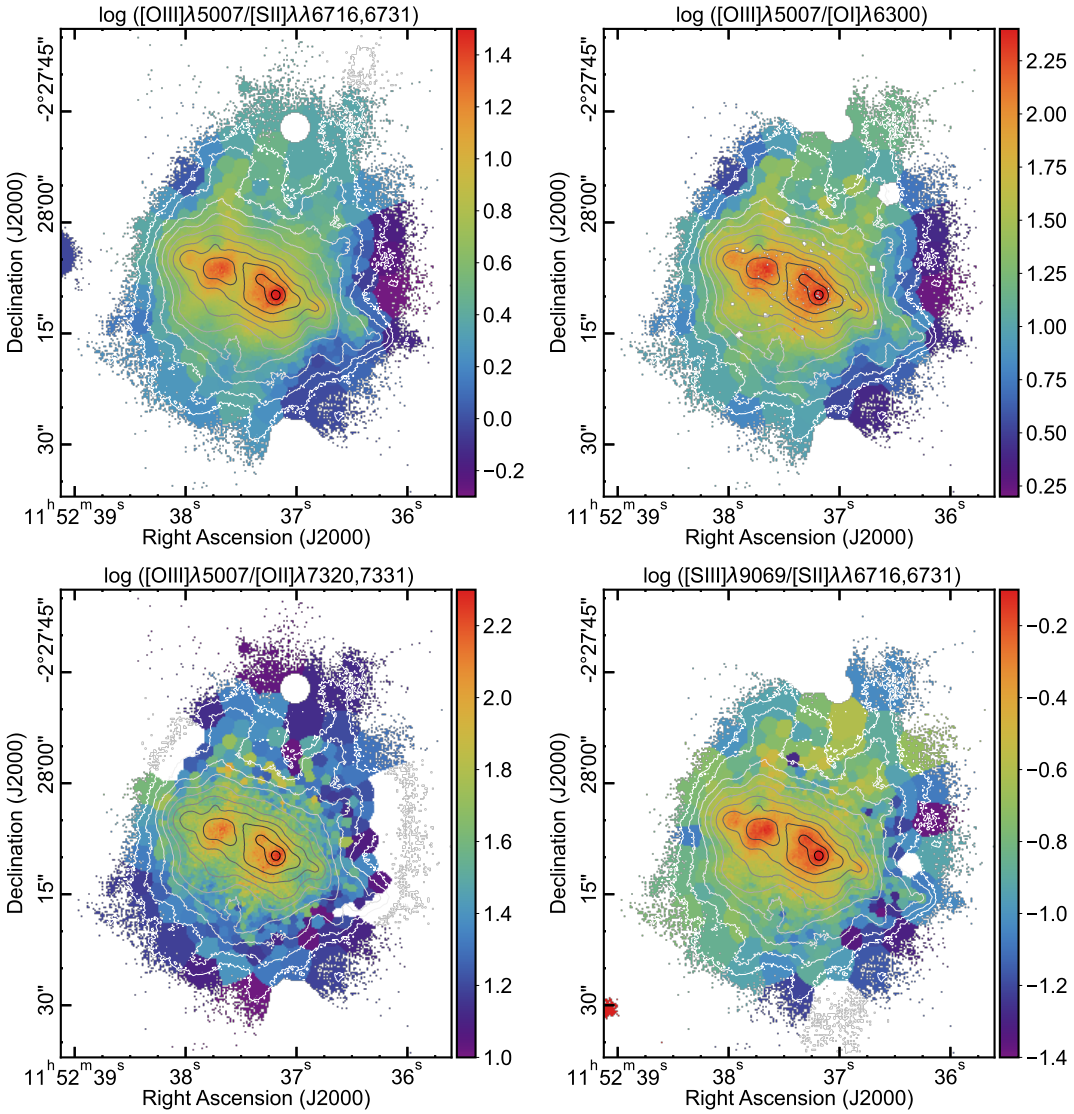

Fig. 14. Maps for the line ratios tracing the ionisation parameter. [O III]/[S II] was introduced by Pellegrini et al. (2012), while the other ratios were used in the diagnostic diagrams presented by Ramambason et al. (2020). North is up and east towards the left.

(e.g. Izotov et al. 2016; Weilbacher et al. 2018; Micheva et al. 2019). Three of those ratios are available within the MUSE spectral range, namely: [S III]λ9069/[S II]$\lambda\lambda$6716,6731, [O III]λ5007/[O I]λ6300, and [O III]λ5007/[O II]$\lambda\lambda$7320,7331. The first two have been already used to explore the possibility of ionising photons escaping from the galaxy (e.g. Ramambason et al. 2020). Regarding a ratio involving [O III] and [O II] emission lines, the most commonly used is the one based on the much brighter [O II]$\lambda\lambda$3726,3728 doublet (unavailable here). Nonetheless, we were able to derive a line ratio map with the [O II]$\lambda\lambda$7320,7331 in a reasonable portion of the galaxy. The extinction corrected maps for all the four observed ratios are presented in Fig. 14. All the four maps basically replicate the structure described for the [O III]/Hβ.

The upper row in Fig. 15 presents the relations between those ratios involving ions of the same element. The [O II]$\lambda\lambda$7320,7331 doublet is a relatively faint feature, detectable here because of the superb MUSE sensitivity. As mentioned above, these lines are not typically used in the literature. Thus, to make the comparison with other works easier, we did not use the direct [O III]λ5007/[O II]$\lambda\lambda$7320,7331 ratio. Instead, we estimated the flux in the [O II]$\lambda\lambda$3726,3728 doublet by scaling the [O II]$\lambda\lambda$7320,7331 with a factor of $\times$48. This factor was determined by calculating the ionic abundance for O^+ from [O II]$\lambda\lambda$3726,3728 for varying fluxes that were compared iteratively with abundances from [O II]$\lambda\lambda$7320,7331 until convergence. Because this ratio contains a derived quantity relying on two faint lines and an assumption in the relation with the [O II]$\lambda\lambda$3726,3728 lines, we also included in the lower row of Fig. 15 equivalent diagrams, this time involving the [O III]λ5007/[S II]$\lambda\lambda$6716,6731. This way, we use a ratio that can be directly derived from strong measured lines, in this case at price of mixing species.

The trend in all the four diagrams is similar. Data points are organised along a (more or less) tight sequence and ordered according to the ionisation degree, with H II-1, being the highest end, and the ear being the lowest end. The [O III]λ5007/[O II]$\lambda\lambda$3726,3728 ratio reaches values of up to ~4.0. These large ratios are comparable to those measured in GP galaxies, Lyman break galaxies at $z \sim 2-3$ and Lyman continuum leakers and ~1−2 orders of magnitude larger than typical star-forming galaxies (Nakajima & Ouchi 2014). A galaxy with

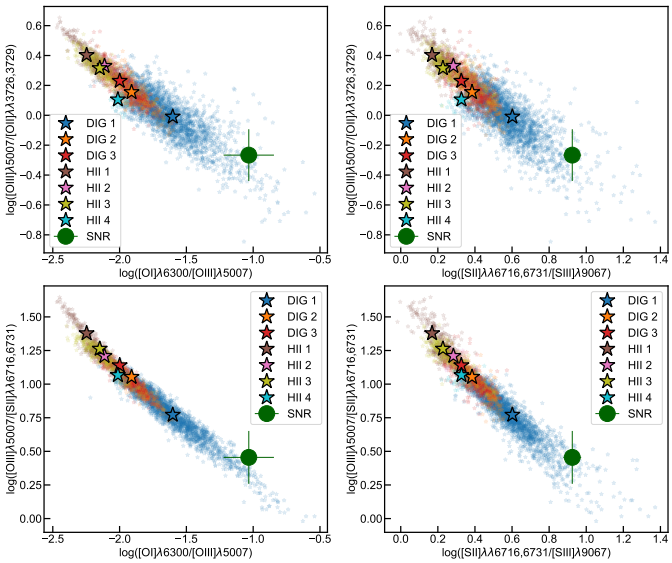

Fig. 15. Position of the individual tiles (small translucent stars) and the regions defined by `astrodendro` (large solid stars) in some additional diagnostic diagrams. *Upper row*: the so called O32−O13 and O32−S23 diagnostic diagrams presented by Ramambason et al. (2020). The [O II]$\lambda\lambda$3726,3229 doublet is not covered by MUSE. Instead, we scaled the fluxes for [O II]$\lambda\lambda$7320,7321 by ×48. The scaling factor was obtained by estimating the needed [O II]$\lambda\lambda$3726,3229 fluxes to obtain the same ionic O^+/H^+ abundances as those reported in the apertures defined in Sect. 3.1. *Lower row*: similar to the upper row but the *y*-axis has been replaced by the [O III][O III]λ5007/[S II]$\lambda\lambda$6761,6731 line ratio. Colour code is the same as in Fig. 13.

such large [O III]λ5007/[O II]$\lambda\lambda$3726,3728 is a good candidate to have a high escape fraction, f_{esc}, even if not all the galaxies with these ratios are necessarily LyC leakers. The ratio for the integrated spectrum of DIG-1 is comparable to those measured in the individual tiles for the horns, and still relatively high ([O III]λ5007/[O II]$\lambda\lambda$3726,3728 ∼ 1), with the area between the horns and the ear having [O III]λ5007/[O II]$\lambda\lambda$3726,3728 of ∼0.50 and ∼0.15, respectively.

4.2.5. Line ratios at local maximum in [S II]/Hα and [O I]/Hα

In Sect. 4.2.3, we mentioned a location in the galaxy with a local maximum in the [S II]/Hα and [O I]/Hα line ratios but barely distinguishable from their surroundings in the [O III]/Hβ line map, and completely undistinguishable in the [N II]/Hα map (see Fig. 12). We discuss its origin in Sect. 5.2. Before that, the emission from this source, which is blended with the overall DIG emission in the galaxy needs to be isolated. We approached this challenge from two fronts, imaging and spectroscopy, making good use of the dual character of IFS data.

For the first approach, we used the reddening corrected flux images to create stamps around the location of interest, and masked that location with a circular mask. Then we created 'DIG stamps', where the emission in the masked area was estimated by 2D interpolation, and we recovered the emission of the source of interest by subtracting the interpolated stamp to the original one. We tried three interpolation methods: linear, nearest, and cubic. The outcome covers a range in satisfaction, depending on the emission line and the interpolation method. In general, it worked better for lines created by ions with low ionisation potential. Regarding the used method, cubic interpolation was the most prone to artefacts. The size of the stamp (3.″8 × 3.″8) and the mask radius (r = 1.″0) were chosen by trial and error looking for a combination minimising the number of spaxel with negative fluxes in the recovered stamps. A particularly challenging line was [O III]λ5007, very bright, but created by an ion with high ionisation potential. The maps for the most relevant lines are presented in Fig. 16 and they confirm the flux excess in an unresolved source in all the lines, especially when looking at low-ionisation ones. We used these images to derive its 'DIG-cleaned' line ratios. The mean values of all the three interpolation methods are displayed in Figs. 13 and 15 with a green solid circle in each graphic. The error bars represent the standard deviation. The large error bar in the [O III]/Hβ (Fig. 13) and [O III]/[S II] and [O I]/[O III] line ratios (Fig. 15) reflect the difficulty of recovering a clean artefact-free map for the [O III]λ5007 line. Values clearly move away from the H II-like zone, and, when looking at the x-axes of the BPT diagrams, the lower the ionisation potential associated with the numerator is, the larger this displacement becomes. Likewise, Fig. 15 shows that low ionisation lines are enhanced over high ionisation lines.

Besides, we recovered the whole spectra associated with the unresolved source. This is even more challenging, since one needs to deblend the information of the unresolved source and the overall DIG emission per wavelength bin. However, it can provide an independent way of estimating the line ratios, and potentially could reveal particularities in the line profiles that help to understand the nature of the unresolved source. As in the previous approach, we chose a stamp around the source of interest and extracted the spectrum in the same circular aperture defined above. Then, we estimated the spectrum of the underlying DIG emission as the median of the spectra in the remaining spaxels, scaled to the size of the circular aperture. Again, the specific size of the working stamp (4.″2 × 4.″2) was chosen by trial and error. Selected portions of the recovered spectrum (and those for the circular aperture and background DIG) are presented in Fig. 17. All the strong emission lines are well recovered, as well as some of the faint lines like the [O II] lines at ∼7325 Å (rest frame). Again, low ionisation lines ([S II] lines, and specially the two [O I] lines) are much stronger than in the underlying DIG emission. Line ratios, as measured from this spectrum, agree with those plotted on the diagnostic diagrams in Figs. 13 and 15 within ∼0.03 dex. Besides, while velocity dispersion in the surrounding DIG is below the MUSE resolving power, we detect marginally broader lines in the recovered spectrum, at least in the reddest lines, where MUSE resolution is larger. We measured a $\sigma_{H\alpha}$ = 1.70 Å that, once corrected from instrumental width (σ_{ins} = 1.06 Å in Hα), implies a linewidth of $\sigma \sim 50\,km\,s^{-1}$.

4.2.6. Equivalent width maps

An additional piece of the puzzle is the equivalent width (EW) for the strongest emission lines. In particular, hydrogen recombination lines can be used to get a rough estimate of the age of the youngest burst of SF. This will be discussed in Sect. 4.3.2. In our case, both, Hα and Hβ could be used to this end. Since nebular Hα is $\gtrsim$3 times stronger than nebular Hβ and stellar Hα can be ∼2.0−2.5 times fainter than stellar Hβ, the precise value depending on the metallicity and age of the stellar population (see e.g. González Delgado et al. 2005), we opted here for using EW(Hα) for that purpose. Additionally, the EW can be used to pin-point those locations where there is an excess of ionised gas emission with respect to that of the underlying stellar

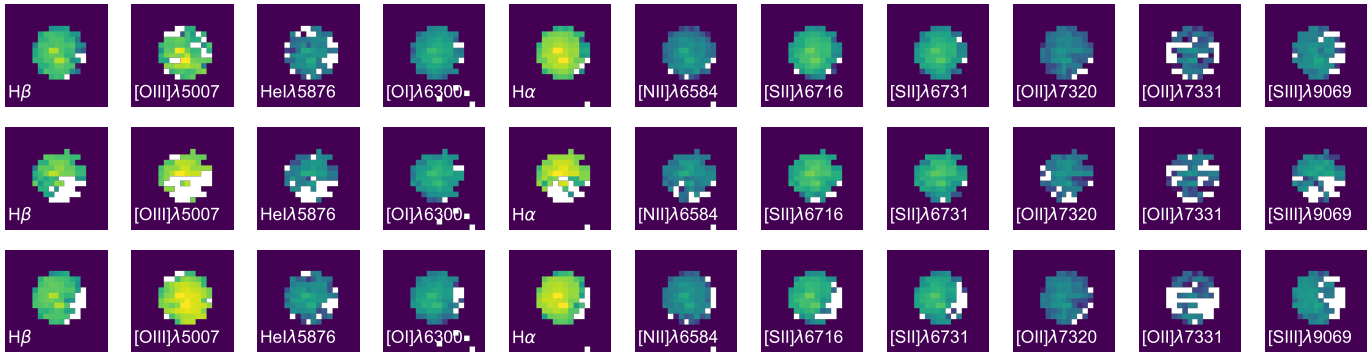

Fig. 16. Stamps with the line emission mapping recovered for the point source, by means of the three interpolation methods (*from top to bottom*: linear, nearest, cubic). The intensity stretch is in logarithmic scale, covers four orders of magnitude and it is the same in every stamp. Spaxels in white have negative fluxes and are artefacts created by the interpolation.

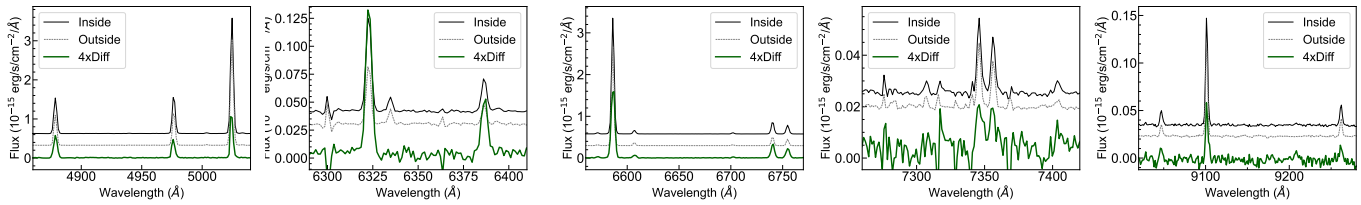

Fig. 17. Selected windows for the spectrum of the SNR candidate. The recovered spectrum is displayed with a dark green thick continuum line. Besides, the total spectrum at the location point source under study ('Inside', black continuous thin line) and the spectrum used to subtract the background emission ('Outside', grey dashed thin line) are also displayed. To better see all the three spectra, the recovered spectrum was scaled by a factor ×4, and the 'Inside' and 'Outside' spectra are offset by ×0.1 and ×0.2 the peak value of 'Inside' in the displayed spectral window.

population. In this manner, one can better delineate ionised gas structures like bubbles, cones, filaments, superwinds and others.

We present the map for the EW(Hα) in the top panel of Fig. 18. Unsurprisingly, the highest values are found in the H II-1 to H II-4 regions, in particular in H II-1, with values of up to ∼1500 Å, and H II-4, with values of ∼800 Å. These values, in particular that for region H II-4, will be discussed in Sect. 4.3.2, together with the ionisation structure as traced by the ratios introduced in Sect. 4.2.4. Here we put the focus on the external parts (i.e. the substructure delineated in the DIG-1 region).

The EW(Hα) in DIG-1 is still high, ranging from ∼10−30 Å in the region between the horns, to values of ∼300−600 Å in two structures relatively symmetric to the horns with respect to the main body of the galaxy, and that bend towards each other and join at the most south-eastern edge of the galaxy. Hereafter, we refer to this set of two structures as 'the beard'. Finally, the so-called horns and ear, present somewhat intermediate values of ∼100−200 Å.

For completeness, we have also included EW([O III]) map (bottom panel of Fig. 18). The galaxy presents a structure pretty similar to the one for EW(Hα), ranging from ∼10 Å between the horns to ∼1400 Å, in H II-1, just modulated by the ionisation structure. De facto, the joint use of these two maps would be almost equivalent to the [O III]/Hβ map presented in Sect. 4.2.4.

When comparing the ionisation structure and the EW maps in here, a noteworthy finding is that both the horns and the beard present similar line ratios, yet while the horns define an open structure and have relatively low EW(Hα) values, the beard is a closed structure with relatively much higher EW(Hα). We discuss these differences in Sect. 5.4, once the kinematic of the system has been introduced, and together with the rest of the observational evidence in these areas.

4.2.7. Ionised gas kinematics

We recovered kinematic information for the overall ionised gas (by means of e.g. Hα and Hβ). Moreover, since we fit individually most of the strong emission lines, we were able to recover independent kinematic information for ions corresponding to high ionisation regions (by means of the [O III] lines) and low ionisation regions (by means of the [O I], [N II], or [S II] lines). The velocity fields for a representative subset of lines is presented in Fig. 19. Besides, the figure also contains the velocity dispersion map once corrected from instrumental resolution, as derived from Hα. The overall stellar velocity field (not shown) was provided by `FADO`, and we used as a reference to which we can compare the velocities of ionised gas. It was completely unstructured, not showing any sign of rotation, any gradient, or any other coherent pattern. To reject the suspicion that this might have to do with the code used to model the stellar population, we derived the stellar velocity field also using two additional codes with similar purpose, `ppxf` (Cappellari 2017) and `PLATEFIT` (Brinchmann et al. 2004), with comparable outcome. Thus, we concluded that the stellar velocity field was simply a consequence of seeing the galaxy (almost) face-on.

The ionised gas presents a different situation. All the velocity maps in Fig. 19 present some structure, with higher (redder) velocities in the east side of the galaxy and lower (bluer) velocities in the west, with a $\Delta v \sim 40\,\mathrm{km\,s^{-1}}$. In that sense these maps are reminiscent of the velocity field for H I (van Zee et al. 1998) that, at a spatial resolution of ∼5″, was interpreted as compatible with solid-body rotation with receding velocities in the

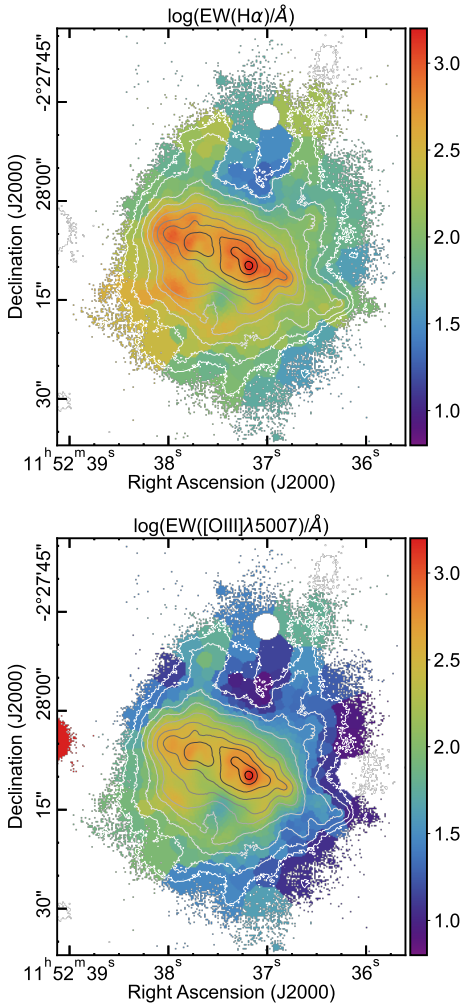

Fig. 18. Maps with equivalent width for the two strongest lines used here, Hα (*top*) and [O III]λ5007 (*bottom*). For reference, the map in Hα flux made by line fitting on a spaxel-by-spaxel basis is overplotted with ten evenly spaced contours (in logarithmic scale) ranging from 1.26×10^{-18} erg cm^{-2} s^{-1} spaxel^{-1} to 1.26×10^{-15} erg cm^{-2} s^{-1} spaxel^{-1}.

east and approaching velocities in the west/south-west. However, the structure in all these maps is much more complex than simple rotation. In the Hα map, the highest (reddest) velocities are not in the east-west direction, as one would expect if the ionised gas were rotating in a similar manner as the neutral gas, but towards the south/south-east. Besides, the northern half of the galaxy presents a clear velocity stratification: the two horns have similar velocities in all the maps, while the space between the horns present redder velocities in the high ionisation lines (here [O III]λ5007, $v_{[\mathrm{O\,III}]} - v_{\mathrm{H}\alpha} \sim 20{-}50\,\mathrm{km\,s^{-1}}$) and bluer velocities in the low ionisation lines (here [S II]λ6716 with $v_{\mathrm{H}\alpha} - v_{[\mathrm{S\,II}]} \lesssim 25\,\mathrm{km\,s^{-1}}$ – not shown –, and [O I]λ6300 with $v_{\mathrm{H}\alpha} - v_{[\mathrm{O\,I}]} \lesssim 45\,\mathrm{km\,s^{-1}}$). This area with velocity stratification presents velocity dispersions well above the MUSE instrumental width. Moreover, the level of stratification (i.e. difference between the velocities of several species) seems correlated with the velocity dispersion. A similar situation but far less dramatic is also visible in the southern half of the galaxy. There, the region marked with a dashed yellow polygon in the velocity dispersion map has $v_{[\mathrm{O\,III}]} - v_{\mathrm{H}\alpha} \sim 10\,\mathrm{km\,s^{-1}}$, $v_{\mathrm{H}\alpha} - v_{[\mathrm{S\,II}]} \lesssim 10\,\mathrm{km\,s^{-1}}$ – not shown –, and [O I]λ6300 with $v_{\mathrm{H}\alpha} - v_{[\mathrm{O\,I}]} \lesssim 20\,\mathrm{km\,s^{-1}}$, and velocity dispersions marginally above what one can resolve at the MUSE spectral resolution. Both regions in the northern and southern half marked with the yellow polygons have large [O I]/Hα line ratios, well beyond the theoretical border proposed by Xiao et al. (2018).

Examples of velocity stratification in the literature are scarce. Velocities differences between the same lines under consideration have been identified in Orion (García-Díaz et al. 2008; Weilbacher et al. 2015). However, this samples areas within an H II region itself and at the sub-pc level, much smaller scales than what we see in UM 462. Monreal-Ibero et al. (2010a) also detected a velocity stratification in NGC 5253, this time at scales of ∼50−100 pc, more comparable to (but still smaller than) the scales sampled here. In that case, the velocity stratification could be explained by a symmetric outflow centred at the main and youngest super star clusters. This does not seem a plausible explanation here since the apex of the northern area with velocity stratification and high velocity dispersion seems located, not at H II-1, the peak of Hα emission and youngest star cluster (see Sect. 4.3) but in between H II-3 and H II-2, where the youngest stars look slightly older. Moreover, the observational evidence is different in the northern and the southern parts of the galaxy. However, the high [O I]/Hα line ratios together with the high velocity dispersion suggest that shocks are having an impact on the ISM in this area. In Sect. 5.4, we discuss a possible scenario able to explain the observed kinematics, together with the rest of observational evidence.

4.3. The stellar populations

4.3.1. General overview

Along with the information for the ionised gas, the MUSE spectra also contain valuable information about the stars. Getting a finely tuned composition of the underlying stellar population, meaning a reliable and detailed 2D star formation history, is a complex task and beyond the goals of the work presented here. Instead, we present here a general overview of the modelling by `FADO` to just get an overall idea of the stellar populations in the galaxy. They are based on the outcome of the modelling described in Sect. 3.2 but were stable against a selection of a slightly different (i.e. more reduced or extended) set of base spectra. The most relevant information is summarised in Fig. 20, that contains maps of the average age weighted by light and mass, and Fig. 21, that contains the light and mass fractions per stellar population for each of the seven areas defined by `astrodendro`. Several pieces of information can be inferred from these figures.

Firstly, there is no need for a stellar population older than ∼1.2 Gyr to model the observed spectra anywhere but H II-3, where `FADO` sees a significant contribution in mass of a ∼4 Gyr stellar population. Micheva et al. (2013) reported broad band colours consistent with an age of the stars in the underlying host galaxy of ∼3−4 Gyr and very low metallicity ($Z \sim 0.001$). This component extended well beyond the area covered by MUSE and it is likely included in the sky emission and thus, subtracted out in most of the apertures. The fact that this is still detected in H II-3 suggests that this old population was more significant there but, given the degeneracies intrinsic to the modelling of the emission of the underlying population, this is a result that should be taken with caution. Nevertheless, relatively old (i.e. ∼1 Gyr) stars are found in any other aperture. This $\gtrsim$1 Gyr stellar population account for most (i.e. ∼60−70%) of the mass over the whole galaxy.

Secondly, Fig. 21 suggests a significant (∼10−30%) contribution to the stellar mass of an intermediate age (∼40−400 Myr)

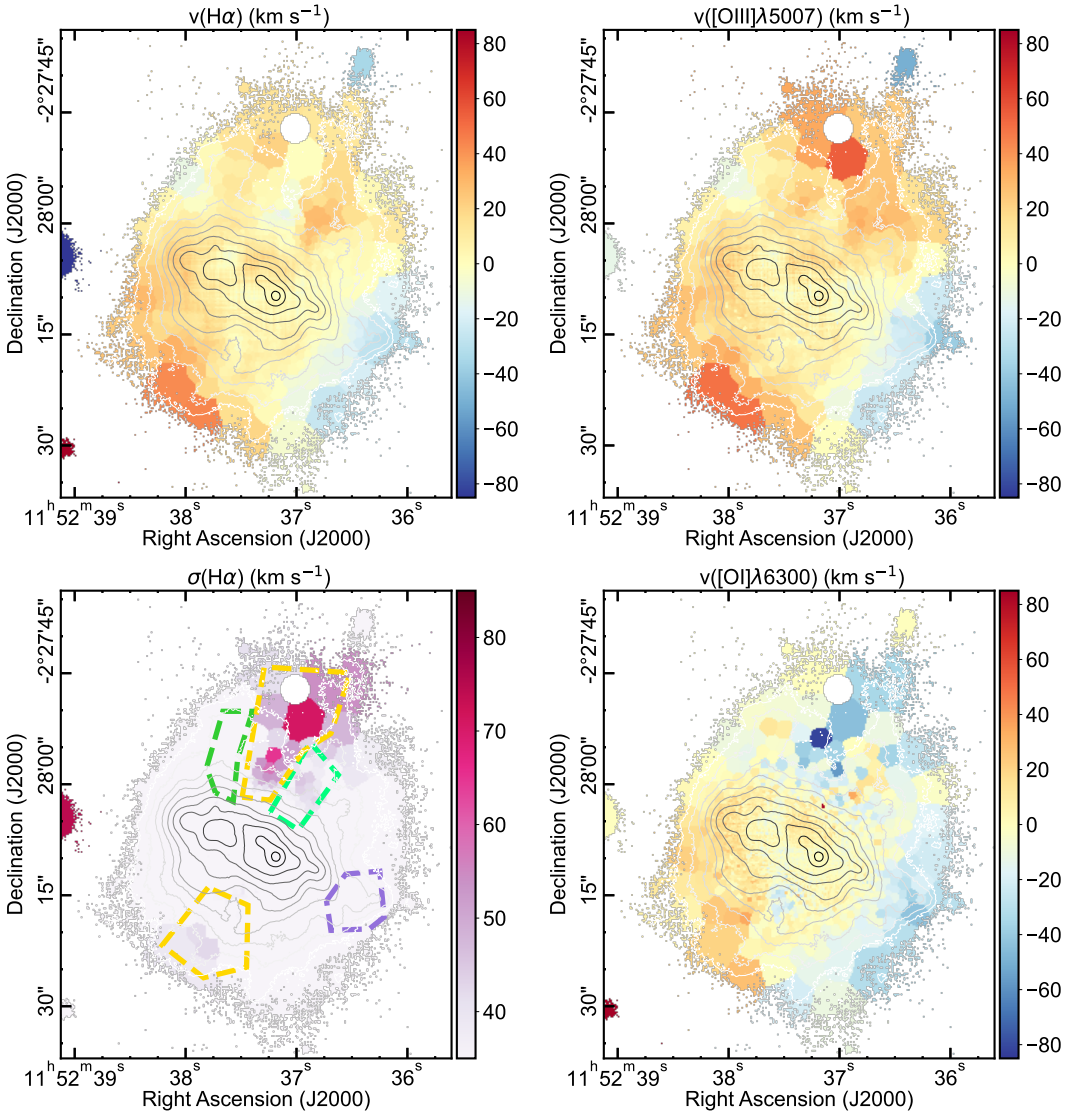

Fig. 19. Representative maps related with the kinematics of the galaxy. *From top to bottom and from left to right*, they are: Hα velocity field, a velocity field for a line tracing the high-ionisation zone ([O III]λ5007), Hα velocity dispersion map corrected for instrumental resolution, velocity field for a line tracing the low-ionisation zone ([O I]λ6300). Values for the velocities are presented as relative to the systemic velocity $v_{\rm sys}$ = 1056 km s^{-1} as derived from the redshift reported in Table 1. For reference, the map in Hα flux made by line fitting on a spaxel-by-spaxel basis is overplotted with ten evenly spaced contours (in logarithmic scale) ranging from 1.26×10^{-18} erg cm^{-2} s^{-1} spaxel^{-1} to 1.26×10^{-15} erg cm^{-2} s^{-1} spaxel^{-1}. North is up and east towards the left.

stellar population in apertures H II-1, H II-2, and their envelopes (DIG-3, but also DIG-2). This intermediate-to-young stellar population extends well in time in H II-2.

Thirdly, FADO also recovers the very young stellar population responsible for the ionising photons. The luminosity of the galaxy in all the apertures is dominated by ∼6 Myr old stars, even if only contributes with $\lesssim$10% of the stellar mass. Besides, most of the apertures but DIG-1 contain even younger stars up to the youngest population included in the modelling by FADO (i.e. 1 Myr, here assimilated to on-going SF). The contribution of this on-going SF is particularly important in H II-1, and to certain extent in its neighbouring apertures (DIG-3 mostly, but also H II-2), and is clearly seen in the luminosity-weighted age map. Finally, this suggests that the most recent SF propagates from the outer to the inner parts of the galaxy (i.e. from DIG-1 to inner apertures), then from east to west, following a path roughly like H II-3 → H II-2 → H II-1. Region H II-4 would be out of this sequence. It also did not formed stars older than ∼1 Gyr. However, it seems to follow an independent story, having formed stars at practically every age, including now, in a relatively continuous manner.

4.3.2. Starburst ages and star formation rates

The emission lines, and in particular Hα, can also be used to characterise the most recent SF. We derived the star formation rates (SFR) for all the seven apertures using the Hα luminosity and the expression:

$$\mathrm{SFR}(M_\odot\,\mathrm{yr}^{-1}) = 10^{-41.27}\times L(\mathrm{H}\alpha)\,(\mathrm{erg\,s}^{-1}) \quad (1)$$

provided by Kennicutt & Evans (2012). They are presented in Table 5. As suggested by the results in Sect. 4.3.1, the SFR is the highest in H II-1. Then, it decreases from west to east and from the inner to the outer parts of the galaxy. We note that DIG-1, the aperture associated to the emission in the outermost parts of the

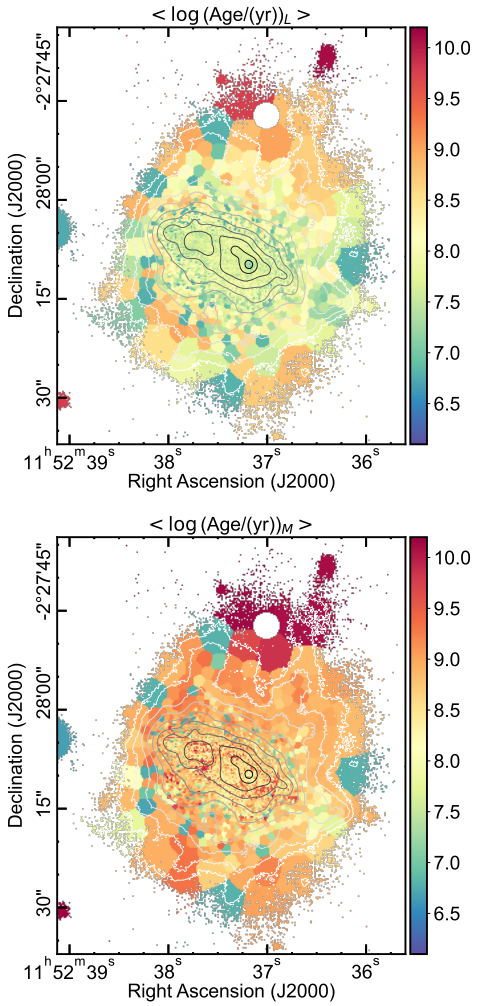

Fig. 20. Maps with the mean age of the stellar population weighted by light (*top*) and mass (*bottom*). For reference, the map in Hα flux made by line fitting on a spaxel-by-spaxel basis is overplotted with ten evenly spaced contours (in logarithmic scale) ranging from 1.26×10^{-18} erg cm^{-2} s^{-1} spaxel^{-1} to 1.26×10^{-15} erg cm^{-2} s^{-1} spaxel^{-1}. North is up and east towards the left.

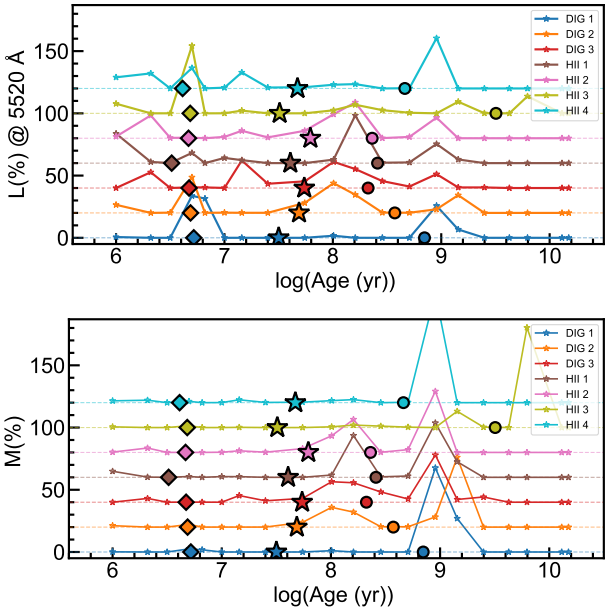

Fig. 21. Light (*top*) and mass (*bottom*) fractions per stellar population as provided by the FADO modelling for the seven areas considered here (small stars). For a given age, the contributions of the two metallicities ($Z = 0.004$ and $Z = 0.008$) have been added. Likewise, to better visualise the light (or mass) fractions for all the seven areas, data have been offset by $+10N$ with N the spectrum number, as indicated by the alphabetically ordering of the labels. Three characteristic values are shown on top of each function: Mean stellar age logarithmic weighted by mass (circles) and by light (stars) together with the estimated age for an instantaneous burst of SF (diamonds), derived from the equivalent width in Hα, and the original STARBURST99 models (Leitherer et al. 1999).

galaxy, contributes with a far from negligible fraction (∼35%) to the total luminosity in Hα.

An alternative path to estimate the youth of the most recent burst of SF, beyond FADO, is using the Hα equivalent widths jointly with the STARBURST99 models[5] (Leitherer et al. 1999). Here, we used the original models for an instantaneous burst of SF, an initial mass function with $\alpha = 2.35$ and upper limit for the star mass of $M_{\rm up} = 100\,M_\odot$ as a baseline. We looked for the estimated age for metallicities $Z = 0.004$ and $Z = 0.008$. The average of both values is presented with diamonds in Fig. 21 and listed in Table 5. Again, the extreme youth of the burst in H II-1 stands out, and even if the burst is young in every aperture, the direction outlined above (increasing age from west to east, from inside to outside) is again outlined.

A comparison of the ages of the youngest bursts of SF at each location and the line ratios tracing the ionisation structure (Sect. 4.2.4) shows how ratios compatible with lower ionisation parameter are found in those locations with older stars, as expected. Not for the first time in this contribution, H II-4 departs from this sequence. It is the location with the second youngest burst and yet, it presents line ratios compatible with lower ionisation parameter than H II-2 and H II-3. We posit here stochasticity as a possible cause of this observational evidence (e.g. Paalvast & Brinchmann 2017; Krumholz et al. 2015). Determining an accurate stellar mass for the young burst at each of the astrodendro locations is beyond the scope of this paper. For Sect. 4.3.1, we simply embraced those provided by FADO, which were enough to get an overview of the global characteristics of the stellar populations. Nonetheless, we can use an approximate estimate of the masses of the youngest stellar populations using the SFR and age provided in Table 5 to explain H II-4's rogue behaviour, assuming that the reported SFRs were constant over the age of the young bursts. Such estimates are largely uncertain but still reliable enough for a discussion in terms of orders of magnitude. In that sense, while the stellar mass in H II-1 and H II-3 is of the order $\sim 10^6\,M_\odot$, that in H II-2 is of $\sim 10^5\,M_\odot$ and the one in H II-4 is even less ($\sim 5 \times 10^4\,M_\odot$). At that range of masses the initial mass function is not adequately sampled in the high-mass end. Thus, it may well happen that the star massive enough to provide the more energetic photons at that location simply did not manage to be born.

Adding up the contribution of all the apertures, the total SFR is $0.17\,M_\odot\,{\rm yr}^{-1}$, larger but comparable with the value reported by Paudel et al. (2018). GP galaxies typically have SFRs ~ 3–$30\,M_\odot\,{\rm yr}^{-1}$ (Cardamone et al. 2009), which is 1–2 orders of magnitude larger than the SFR here. In every other aspect considered so far (e.g. gas metallicity, electron density and temperature and emission line ratios), UM 462 is similar

[5] https://www.stsci.edu/science/starburst99/docs/default.htm

Table 5. Basic properties of the recent SF in the regions defined by `astrodendro`.

Property	DIG 1	DIG 2	DIG 3	H II 1	H II 2	H II 3	H II 4
$L(\mathrm{H}\alpha)$ [(a)]	112.49±0.56	22.48±0.10	58.71±0.28	84.41±0.44	4.57±0.03	38.30±0.16	3.51±0.01
SFR [(b)]	60.41±0.30	12.07±0.05	31.53±0.15	45.33±0.23	2.45±0.01	20.57±0.08	1.88±0.01
Σ_{SFR} [(c)]	1.67±0.01	15.71±0.07	26.90±0.13	66.08±0.34	43.14±0.26	28.99±0.12	18.84±0.07
$\mathrm{Age}_{\mathrm{SB99}}$ [(d)]	5.21	4.86	4.71	3.26	4.66	4.83	4.11

Notes. [(a)]In units of 10^{-38} erg s^{-1}; [(b)]In units of 10^{-3} $M_\odot$ yr^{-1}; [(c)]In units of 10^{-2} $M_\odot$ yr^{-1} kpc^{-2}; [(d)]In Myr.

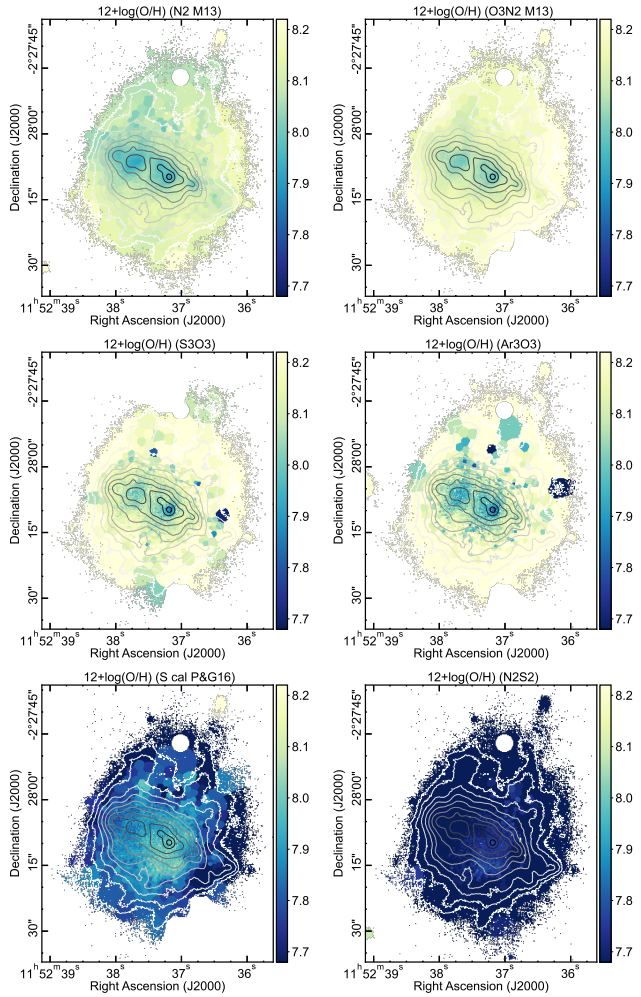

Fig. 22. Maps of total oxygen abundance derived by means of different strong line methods. *Upper row*: calibrations by Marino et al. (2013) for the N2 (*left*) and the O3N2 (*right*) methods. *Middle row*: calibrations by Stasińska (2006) for the S3O3 (*left*) and Ar3O3 (*right*) methods. *Lower row*: S calibration by Pilyugin & Grebel (2016) (*left*) and N2S2 calibration by Dopita et al. (2016) (*right*).

to the GP galaxies. This suggests that GP galaxies could be the brightest and most vigorous end of a galaxy population at $z \sim 0.1-0.2$ where objects like UM 462 may be common. In turn, UM 462 would be representative of the faint end of the GP galaxies distribution and thus allows us to study the processes taking place in faint GP galaxies. Up to now, at $z \sim 0.1-0.2$, studies similar to those existing for the brighter relatives were not possible but they may be common with the advent of the *James Webb* Space Telescope (JWST). Such studies will surely benefit from the results found for this and similar galaxies in the Local Universe.

5. Discussion

5.1. Strong line methods to derive oxygen abundance

Deriving abundances by means of the direct method in extragalactic sources is certainly challenging, since it needs a determination of T_e which, in turns, depends on faint auroral lines (e.g. here [N II]λ5755 or [S III]λ6312), specially in low surface brightness diffuse component of the ionised gas. Instead, it is more common to use certain combinations of strong emission lines with more or less well established empirical and/or theoretical calibrations: the so-called strong line methods. Several of the lines involved on these methods are observed all over the galaxy. Thus, these data constitute a good opportunity to assess their performance.

One of the most used indexes is N2 = log([N II]λ6584/Hα), first proposed by Storchi-Bergmann et al. (1994). It seems handy for studies at high redshift, since it involves only two lines that are very close in wavelength. However, it should be handled with care since it is sensitive to relative atomic (nitrogen) abundances, in particular at low metallicity (Morales-Luis et al. 2014). Another common index is the O3N2 = log(([O III]λ5007/Hβ)/([N II]λ6584/Hα)), proposed by Alloin et al. (1979). At least in very nearby H II regions, it seems less sensitive to variations in the ionisation parameter (e.g. Monreal-Ibero et al. 2011) but it involves a larger number of lines spread over a wider spectral range. The oxygen abundance maps for these indexes using the calibration proposed by Marino et al. (2013) are presented in the upper row of Fig. 22. Similar maps are obtained with other calibrations (e.g. Bian et al. 2018; Pérez-Montero et al. 2021).

Besides, Stasińska (2006) proposed two additional indexes that behaved well when determining the overall metallicity of the galaxy (Ar3O3 = log([Ar III]λ7135/[O III]λ5007) and S3O3 = log([S III]λ9069/[O III]λ5007)), even if their uncertainty is somewhat larger (~0.3 dex). The oxygen abundance maps using these indexes are presented in the central row of Fig. 22. All the four maps are presented with a scale covering the same range as the oxygen abundance map in Fig. 10, derived through the direct method, to make easier the comparison between these figures. Given the strength of the involved lines, uncertainties for these calibrators are dominated by the calibration method at play, not by the line measurements and are within the range of ~0.05−0.30 dex, depending on the index.

Overall, the metallicity distribution in all these four maps is radically different to the one presented in Fig. 10. While the galaxy is seen as presenting an homogenous abundance in oxygen when the direct method is used, it would have been interpreted as chemically inhomogeneous (to a different degree) if any of these four strong line methods had been used.

Assuming the metallicity derived from the direct method as the 'true metallicity', we can evaluate the accuracy of each of these methods in the different parts of the galaxy by comparing

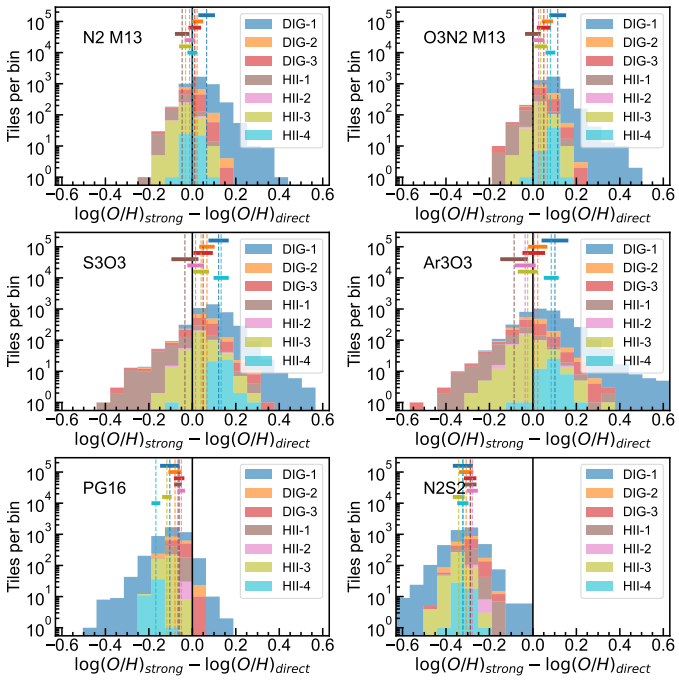

Fig. 23. Histograms with the difference between the oxygen abundance, 12 + log(O/H), as derived from different strong line methods and the direct method, in the different regions defined with `astrodendro`. Vertical dashed lines denote the mean of a given distribution while the length of thick horizontal bands is the standard deviation. The order of the rows and columns is the same as in Fig. 22.

the metallicity as derived from a strong line method against the one from the direct method. This is shown as histograms in Fig. 23. In general, all the four methods tested here predict reasonably well the metallicities in the H II regions. This is not surprising since they were calibrated using H II regions (or at the very least, whole galaxies dominated by the emission of their H II regions). However, there are nuances. The dispersion is clearly lower for the N2 and O3N2 indexes than for the S3O3 and Ar3O3 ones. In particular, these two last indexes overestimate the metallicity in H II-4 by $\gtrsim$0.1 dex. This discrepancy is even stronger when looking at the tiles corresponding to the DIG apertures, in particular DIG-1, that traces the outermost part of the galaxy. On average, all the ratios predict abundances $\gtrsim$0.1 dex larger in DIG-1, but the further from the main site of SF one goes, the larger the difference becomes, reaching values of $\gtrsim$0.2 dex in the N2 and O3N2 methods, and $\gtrsim$0.3 dex in the S3O3 and Ar3O3 in a significant area of the galaxy.

The underlying cause of these discrepancies can be explained by the same effect, even if the impact depends on the ratio one is looking at. ISM in the DIG is expected to be dominated by low excitation lines, thus it is not surprising that those indexes involving only high excitation lines (i.e., the S3O3 and Ar3O3, with ionisation potentials of 23.34 for S^{++} eV, 27.63 eV for Ar^{++}, and 35.12 eV for O^{++}) do not adequately trace the metallicity there. That metallicity is preferentially overestimated can be understood by the fact that O^{++} has larger ionisation potential than S^{++} or Ar^{++}. Of course, when looking along the line of sight of a spaxel in the DIG, contribution of the different zones (using Garnett's nomenclature) with the whole range of ionisation degree is expected. However, the relative contribution of the high-ionisation (and better traced by O^{++} over S^{++} or Ar^{++}) zone is expected to be less important in the DIG, implying higher S3O3 or Ar3O3 indexes that would translate in higher metallicities.

Something similar (but more subtle since also a low excitation line is involved, [N II]λ6584) seems at play in the other two indexes. Here, the discrepancies between the direct and the strong line methods, when looking at the DIG are smaller ($\lesssim$0.1 dex). In the particular calibrations tested here the N2 index provides metallicities in slightly better agreement than the O3N2 index.

The last rows in Figs. 22 and 23 contains the results for two additional indexes using different set of lines. On the left column on that row, we present the results for the *S* calibration as proposed by Pilyugin & Grebel (2016), that makes use of a combination of oxygen, sulphur and nitrogen lines. This index was conceived to take into account the ionisation parameter, and it is, de facto, the one that finds the most uniform metallicity distribution of the indexes tested here, with differences <0.2 dex between H II-1 and H II-4 and comparable metallicities in the H II region and the surrounding DIG. However, it seems to globally underestimate the metallicity by ~0.1 dex. This may be attributed to the somewhat low relative nitrogen-to-oxygen abundance, that is at the lower end of the log(N/O) values used by Pilyugin & Grebel (2016) to calibrate this index.

Finally, on the right column on that row, we present the results for an index proposed by Dopita et al. (2016), and that makes use of a combination of the [N II], [S II], and Hα emission lines (here referred as N2S2 index). This was, in principle, a handy choice of lines for high redshift studies since they fall within a short spectral range (<300 Å), thus being independent of any extinction correction and relatively easy to observe with a single observational set-up. However, this is the index that clearly perform the worst of all those tested here, underestimating the metallicity by ~0.4 dex. This index was calibrated using photoionisation models. Large discrepancies between the abundance values produced by empirical and theoretical calibrations of strong line methods are well acknowledged in the literature (e.g. Kewley & Ellison 2008), and in general, an empirical metallicity scale is preferable (Pilyugin & Grebel 2016). The experiment presented here with this one galaxy supports this statement. A possible origin for this discrepancy can be the relative abundances assumed for the calibration of N2S2 index. At the oxygen abundance for UM 462, a log(N/O) $\sim$ −1.4 was assumed for the calibration, larger by ~0.3 dex than the log(N/O) measured here.

Having a reliable diagnostic to determine metallicities at any point of a galaxy is essential to identify chemical inhomogeneities that can be associated with in and outflows of material. The choice of the index, systematics of the specific calibration, the characteristics of the target under study (i.e. H II regions or DIG, moderate star-forming galaxy or extreme starburst), and the level of contrast one wants to achieve when detecting chemical inhomogeneities, are all aspects that should be taken into consideration. Ultimately, this has an impact on our understanding of the mechanisms that regulate the processes of galaxy enrichment and chemical evolution. The exercise presented here, involving a single galaxy and a single metallicity, illustrates that there is still some way to go. A comparison between the direct method and the *S* calibration in Haro 11 points towards the same direction (Menacho et al. 2021). In that sense, a similar exercise on a sample of galaxies covering a range of metallicities seems imperative. In parallel, new techniques that do not rely on the detection of auroral lines to obtain an estimate of the electronic temperature reveal themselves as promising alternative (e.g. Kreckel et al. 2022; Fernández et al. 2023).

5.2. A supernova remnant candidate

In Sect. 4.2.5, we measured the intrinsic line ratios and line width of a local maximum in the [S II]/Hα and [O I]/Hα maps. Here, we discuss the nature of the source causing this emission. There are several mechanisms that can produce line ratios departing from the typical values expected from H II regions, and with enhanced forbidden line ratios. Because of its point-like nature, we can reject those usually associated with extended DIG emission like post-AGB stars (Binette et al. 1994). Likewise, we can also discard structures larger than ∼150 pc like large bubbles and shells. Besides, an active galactic nucleus can be rejected right away because of its non-nuclear nature. Possible point-like causes for the observed line ratio are planetary nebulae (PNe) and Supernova remnants (SNRs), both of stellar origin or, being more specific, the corpse left after the death of different kinds of stars. PNe have been detected with MUSE in galaxies at distances similar to that of UM 462, and even beyond (Kreckel et al. 2017; Roth et al. 2021), and do have strong forbidden lines. However, this applies to both, high and low ionisation lines. Looking at the original BPT diagrams, PNe typically have log([N II]/Hα) ∼ 0.0−0.5 dex and log([O I]/Hα) ∼ −0.5−0.0 dex, much larger than the values we measured for our source, but admittedly in the same direction. However, the most prominent optical line in a PN is usually [O III]λ5007. In the original BPT diagrams, PNe typically occupied the locus with log([O III]/Hβ) $\gtrsim$ 1, larger than any ratio we measure at any place in UM 462. This is even more true in the emission attributed to the source under discussion.

A last possibility is that this emission could be caused by a SNR. This, in principle, should be detectable with MUSE data at these distances (Cid Fernandes et al. 2021). The expected size of a SNR is ∼40 pc (Roth et al. 2018), thus compatible with an unresolved source at the distance of UM 462. Historically, a log([S II]$\lambda\lambda$6716,6731/Hα) = −0.4 have been considered the canonical lower limit for a typical SNR spectrum (Mathewson & Clarke 1973; Fesen et al. 1985). We measured a log([S II]$\lambda\lambda$6716,6731/Hα) ∼ −0.49 dex. Thus, strictly speaking, our line ratios do not comply with this criterion, although they are quite close. However, this criterion is based on only one ratio and seems too strict. As discussed by Kopsacheili et al. (2020), it might miss SNRs with relatively low shock velocities, characteristic of older SNRs, for instance. These authors derived additional criteria involving sets of two or three line ratios by means of machine learning techniques. Our pair of log([S II]$\lambda\lambda$6716,6731/Hα) and log([O I]λ6300/Hα) are compatible with the criterion provided by these authors. Besides, assuming a relation between the [O II]$\lambda\lambda$7320,7331 and [O II]$\lambda\lambda$3726,3729 as in Sect. 4.2.3, our line ratios also comply with the criterion proposed by Fesen et al. (1985) based on the Hβ, [O II]$\lambda\lambda$3726,3729, and [O I]$\lambda\lambda$6300,6363 emission lines. Our [N II]$\lambda\lambda$6548,6584/Hα line ratio is somewhat lower than the values reported in these works. However, metallicity may play a role here. Payne et al. (2007, 2008) present [N II]$\lambda\lambda$6548,6584/Hα, [S II]$\lambda\lambda$6716,6731/Hα, [O I]$\lambda\lambda$6300,6363/Hα line ratios for a sample of SNR in the Magellanic Clouds, the closest star-forming galaxies with metallicities similar to that of UM 462. Their ratios compare well with those measured here. Besides, we measure a ratio of the two sulphur lines of 1.35 ± 0.02, comparable to the line ratios measured for SNR in the Magellanic Clouds (Payne et al. 2007, 2008). The corresponding density, as derived in Sect. 4.2.1 is n_e([S II]) = 100^{+20}_{-15} cm^{-3}, smaller but comparable to the median n_e([S II]) of 530 cm^{-3} reported by Payne et al. (2008). We could also estimate an electron temperature from the sulphur lines of $T_e = 11\,000^{-3500}_{+2900}$ K, somewhat lower than the one determined for the environmental ISM. All in all, the most plausible of all the ionisation mechanism considered to explain the emission at RA (J2000) = 11:52:37.8 and Dec (J2000) = −02:28:03.0 is a SNR. Interestingly enough, such a SNR, just at the outskirts but not in the regions H II-1 – ...– H II-4 supports the scenario suggested in Sect. 4.3.1 where the most recent SF propagates from the outer to the inner parts of the galaxy (and then from east to west).

5.3. The presence of Wolf-Rayet stars in UM 462

In Sect. 4.3, we presented an overview of the stellar populations and saw how the FADO modelling suggested that the most recent SF propagates from east to west. An additional tracer of the youngest stellar populations is the presence of spectral features characteristics of Wolf-Rayet (WR) stars. These are massive ($M \gtrsim 25\,M_\odot$) stars at certain short-duration stages after abandoning the main sequence (see Crowther 2007, for a review) and can be used as a precise clock to estimate the age of young stellar population.

The taxonomy of WR stars is rather complex and relies on the characteristics (presence, relative strength and shape) of certain emission features in the stellar spectra. When studying unresolved stellar populations, the classification is simplified to the maximum, and usually only two main classes are considered: nitrogen WR stars (WN stars), with strong helium and nitrogen lines and where the star shows the products of the CNO burning, and carbon (or oxygen) stars (WC and WO stars) with strong helium, and carbon or oxygen lines, and where the star shows the products of He burning. During its life, a given massive star may or may not pass by some of the stages associated to the different types of WR stars, depending on a variety of aspects such as its initial mass, metallicity, amount of rotation or whether it is an isolated star or in a binary system (Crowther 2007). Both, binarity and rotation, favour the appearance of WR features, lowering the lower mass limit for an star to go through the WR phases and making them last longer (e.g. Meynet & Maeder 2005; Eldridge et al. 2008; Georgy et al. 2012).

Spectral features characteristics of WR stars are fainter at lower metallicities (Hadfield & Crowther 2007) but by no means inexistent. The most important WR features used in extragalactic astronomy are a bump around 4650 Å, i.e. the blue bump, which is mainly but not always characteristic of WN stars, and a fainter bump around 5808 Å, i.e. the red bump, characteristic of WC stars. There are plenty of examples for detection of these features in BCDs or galaxies with metallicities similar to that of UM 462 (e.g. Guseva et al. 2000; López-Sánchez & Esteban 2010).

Given the youth of the most recent burst of SF, one would expect the presence of such features in UM 462. However, this has not firmly proven so far. On the one hand, based on the detection of a broad He IIλ4686 emission line, as well as the detection of the Si IIIλ4565 and the He I/N IIλ5047 spectral features, Guseva et al. (2000) suspect the presence of WR in the galaxy. On the other hand, James et al. (2010) did not find evidence of those features in their data, even if they used several extraction apertures in an attempt to minimise the dilution of the WR features by the stellar continuum.

The strongest of the WR features, the blue bump, is not covered with the present data. Nonetheless, we can contribute to clarify this issue by looking for the red bump. To do so, we pinpointed the WR emission following a similar methodology

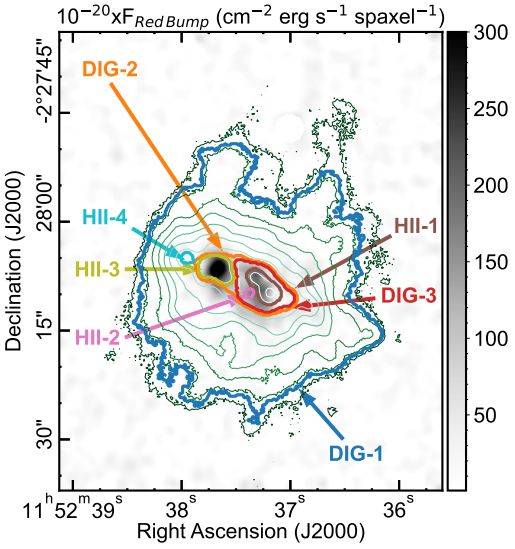

Fig. 24. Map showing the location with excess of emission at the wavelengths corresponding to the red bump (5760−5860 Å, rest-frame). For reference, the map in Hα flux made by line fitting on a spaxel-by-spaxel basis is overplotted with ten evenly spaced contours (in logarithmic scale) ranging from 1.26×10^{-18} erg cm^{-2} s^{-1} spaxel^{-1} to 1.26×10^{-15} erg cm^{-2} s^{-1} spaxel^{-1}. Likewise, the different regions and areas discussed along the work are marked with the same colour and line code as in Fig. 3. North is up and east towards the left.

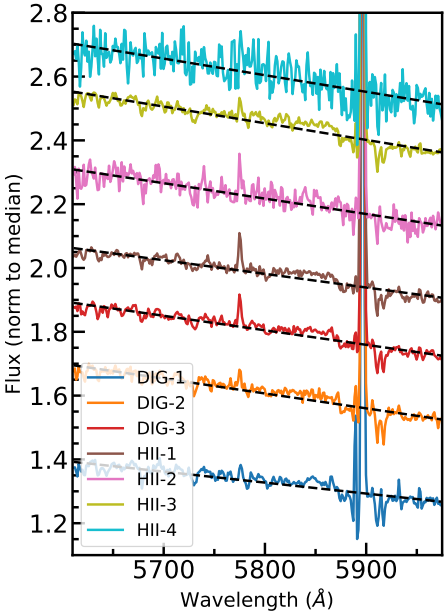

Fig. 25. Zoom of the same spectra displayed in Fig. 4 in the spectral range corresponding to the red bump. To guide the eye, a linear fit to the local continuum is also displayed with a black dashed line for each spectrum.

as that described by Monreal-Ibero et al. (2017). Basically, we created a map for the red bump emission by simulating the action of narrow tunable filters at the bands proposed by Brinchmann et al. (2008), corrected for the redshift of the galaxy, and applied those to the Galactic extinction corrected data cube. We did not convolve the resulting image with a Gaussian filter since nothing was gained with that because of the poor seeing of the data.

The resulting map is presented in Fig. 24. There is a clear flux excess at the location of aperture H II-3, as well as in some areas of H II-1, and DIG-3. Additionally, there might be some marginal flux excess in the part of DIG-1 closest to the centre of the galaxy. A zoom of the spectra presented in Fig. 4 in the spectral range of the red bump is presented in Fig. 25. To guide the reader, we added a 1-degree polynomial fit to the local continuum in each spectrum. The bump is clearly seen in apertures H II-3, H II-1, and DIG-3. Besides, there may be a marginal detection in DIG-2 and DIG-1. Thus, these data support the presence of WR stars in the galaxy. Because of the poor seeing and the inaccessibility of the blue bump, we did not attempt to further isolate the WR emission and estimate the number of WR stars.

A point worth mentioning is that most of the red bump emission is not associated with the youngest burst of SF, H II-1, but to the somewhat older H II-3. Differences in the distribution of the blue and red bumps emission have been used in the past to trace the propagation of the most recent SF within a galaxy with the youngest stellar populations at those places where only the blue bump is detected, then going towards somewhat older stellar populations in those places where both bumps (or only the red bump) are detected (Westmoquette et al. 2013; Monreal-Ibero et al. 2017; Gunawardhana et al. 2020). In that sense, the red bump detection together with the results presented in Sects. 4.3.1 and 4.3.2 motivate us to hypothesise the presence of WR stars, and in particular WN stars, in H II-1, and claim loudly for 2D spectroscopic data at high spatial resolution to confirm (or reject) that hypothesis. That is: mapping the blue bump in the centre of UM 462, and carrying out a proper census of the WR population in the galaxy would allow to strength (or reject) the scenario of east-west propagation of the SF.

5.4. The horns, the beard and the story behind them

In Sect. 4.2.3, we introduced two ∼1 kpc-long structures towards the north of the galaxy, clearly delineated in the maps with ratios involved in the BPT diagram. We nicknamed them 'the horns'. Similarly, we identified a closed, almost loop-like structure in Sect. 4.2.6. We named it 'the beard'. Here, we discuss the origin of both structures based on the join observational evidence collected through this work.

The horns. With an angle between them of ∼25°, these two structures frame the only area in the galaxy with velocity dispersions clearly high enough to be measured at the MUSE spectral resolution and displaying velocity stratification. They have relatively high EW(Hα), thus suggesting larger concentration of ionised gas, and line ratios tracing relatively high ionisation parameter (even if not as high as the main site of SF).

We posit here that this set of structures represents the effects of the stellar feedback in the galaxy at a relatively advanced stage, as the 2D projection (in the plane of the sky) of a fragmented super-bubble, where the galaxy has already lost part of its ISM. The wall of such a fragmented super-bubble is seen edge-on at the location of the horns, while in between the horns, we see the integrated emission of the back and front side of the wall, probably dominated by the emission of the front side.

This would be consistent with higher velocity dispersions just in the middle point between the horns then decreasing when moving in the E-W direction towards the horns, exactly as observed. In this scheme, one would expect higher ionisation species being preferentially found in the inner side of the wall, while lower ionisation species would preferentially be located in the outer side of the wall. Under the assumption that the

emission in between the horns is dominated by the front side of this wall, the kinematics, with redder velocities for [O III]λ5007 and bluer velocities for [O I]λ6300, supports this picture.

The scenario presented here is only sketched but already allows to make some predictions that can be used to plan spectroscopic observations at high spectral resolution, able to reinforce, refine, or refute it. These would not need to map the whole area but should sample, at least, the horns and the area in between at one or two locations, and provide information for at least one hydrogen recombination line, one line tracing high excitation (e.g. [O III]) and one line tracing low excitation (e.g. [N II], [O I], or [S II]). For the scenario proposed here to be valid, such observations should deliver line splitting, with larger split in the middle point between the horns, and decreasing when moving towards the horns, where there should be no splitting at all. Likewise, this splitting should be larger for the low ionisation lines than for the high ionisation lines. Finally, for a given line the blue component should be stronger than the red component.

Perhaps the closest example to the stratification found here is presented by Menacho et al. (2021), who also found kpc-scale areas in Haro 11 with velocity difference between the Hα and [N II] emission lines. These were also explained as perhaps remnants of a kpc-scale superbubble whose break out might have created a filamentary structure. The findings in this area of UM 462 suggest a similar mechanism at play here, where the system has managed to carve a passage through which, perhaps, ionising photons from the youngest generation of stars could escape from the galaxy.

The beard. This structure presents some similarities with the horns (e.g. line ratios), but its interest lies precisely in the differences: (i) it is a closed structure (as opposed to open); (ii) it is somewhat smaller in size; (iii) it has EW(Hα) values larger than the horns by a factor ∼2−3; (iv) the area encircled by the structure have velocity dispersions just marginally above what it is possible to resolve with MUSE; (v) it is at a location of the galaxy with much more atomic gas (van Zee et al. 1998).

Here we propose that this could be a location where the effects of the stellar feedback are at a somewhat earlier stage than in the northern part of the galaxy. The ionised gas structure fruit of the stellar feedback is still (almost) unbroken and the (ionised) gas is still retained within the galaxy. An observational experiment as the one designed above could also be set up for this structure. However, reinforcing, refining of refuting this proposal would be more difficult than the one for the northern part of the galaxy since velocity differences between the components are expected to be smaller, and thus a putative line splitting more difficult to detect.

When comparing the observational evidence presented here and found in GP galaxies, an outstanding difference is the lack of clear broad emission line wings in UM 462 while these seem common in the GP galaxies (Amorín et al. 2012). There are three non-exclusive reasons that may explain this difference. On the one hand, if UM 462 actually represents the faint end of the GP distribution, it might well be that the effects of the stellar feedback, even if existing, are not as vigorous as in GP galaxies. On the other hand, given the spatial resolution at which GP galaxies have been observed so far, the observed emission lines in these galaxies are integrated over considerable areas, and these broad components may just be the sum of the complex large scale gas motions within them. High fidelity spatially resolved observations at high-spatial resolution of GP galaxies, now possible with the JWST, could shed light on the sort of (kinematic) substructures at place in GP galaxies. The third possibility is that these broad components were actually present in UM 462, just challenging to be rescued. As we mentioned in Sect. 3.3, both [O III] emission lines display a broad component at their base in the seven `astrodendro` spectra. However, this is at a level comparable to the wings of the MUSE LSF, and thus not attributable with certainty to the target. Delicate experiments as done with PMAS data for Mrk 71/NGC 2366 (Micheva et al. 2017), or by propagating the shape of the LSF (as measured from the arc lines) to the apertures under study, could shed light into this issue and constitute a nice avenue for future research.

6. Conclusions

We present here a unique detailed spectroscopic study on a nearby BCD galaxy resembling the GP galaxies, UM 462. For that, we made use of MUSE data mapping most of the galaxy (i.e. an area of ∼55″ × 40″ or ∼3.8 kpc × 2.8 kpc) with deep wavelength coverage from 4750 Å to 9300 Å. This allowed us to characterise the physical and chemical properties of the ionised gas, as well as get an overview on the properties of the stellar population in the galaxy. Our main results are:

1. The Hα/Hβ line ratio is consistent with no extinction in most of the galaxy. The only exceptions are the main site of SF with c(Hβ) ∼ 0.4 and some secondary sites of SF with c(Hβ) ∼ 0.2. As expected, the overall stellar population suffers from less extinction than the ionised gas.
2. Electron densities as traced by the [S II] emission line ratio are below the low density limit all over the galaxy but in the main site of SF, with n_e([S II]) ∼ 100 cm^{-3}. Although uncertainties are large, electron densities as traced by the [Cl III] line ratio seem higher but again below the low density limit for this diagnostic.
3. Electron temperatures by means of the [S III], [N II], and He I lines at specific apertures were derived. Median T_e decreases according to the sequence [S III] → [N II] → He I. Furthermore, T_e([S III]) values are ∼13 000 K, and uniform within the uncertainties over an area of ∼20″ × 8″ (∼1.4 kpc × 0.6 kpc). This is comparable to the T_e's measured in GP galaxies.
4. We derived several ionic and elemental abundances. Regarding helium, ionic abundance, He^+/H^+, ranges from ∼7.7 × 10^{-2} to ∼8.2 × 10^{-2}, which is compatible with the values previously reported. Values become lower when going towards the outermost part of the galaxy, suggesting a larger contribution of neutral helium there.
5. Regarding light elements, we mapped oxygen ionic and elemental abundances by means of the direct method. Total oxygen abundances were 12 + log(O/H) ∼ 8.02, in agreement with the previous reported values. Within the uncertainties, there is no O/H inhomogeneity in UM 462. We also derived abundances for nitrogen, sulphur, argon, and chlorine in selected apertures, which were compatible with values available in the literature. Regarding nitrogen, we mapped its relative to oxygen abundance, N/O. We found a mild ($\lesssim$−0.2 gradient of log(N/O) crossing the galaxy in the north-east to south-west direction (i.e. H II-4 with log(N/O) ∼ −1.8 → H II-1 with log(N/O) ∼ −1.6. This is of the order of the uncertainties, and thus still compatible with homogeneity in nitrogen.
6. Several strong line methods to derive metallicities were put to test by comparing their predictions with those by the direct method. In general, they performed well at the H II regions and not that well at the DIG. The N2, O3N2, S3O3, and Ar3O3 indexes detected chemical inhomogeneities, to a different extent depending on the index, not present according

to the direct method. The so-called S calibration provided a somewhat more homogeneous oxygen abundance, but it was lower by ∼0.1 dex than the one derived by the direct method. The only tested index based on models, N2S2, largely underestimated the metallicity in the galaxy (i.e. by ∼0.4 dex). A similar exercise on a sample of galaxies covering a range of metallicities seems imperative to identify the best metallicity diagnostic valid all over a given galaxy, since this ultimately has implications on our ability to identify chemical inhomogeneities and to understand the galaxy chemical evolution.

7. We mapped several strong line ratios used for plasma diagnostic. Those involved in the BPT diagrams are mostly compatible with gas photoionised by massive stars. However, a systematic excess in the [O I]/Hα ratio is found. This suggests an additional mechanism or a specific configuration of the relative distribution of gas and stars.We note that [N II]/Hα, [S II]/Hα, and [O I]/Hα line ratios were the lowest in the main sites of SF, and they increased when going towards the external parts of the galaxy. Furthermore, [O III]/Hβ presented the reversed distribution. The galaxy presented two structures, referred to as 'the horns' here, towards the north with the highest [O III]/Hβ ratios, with the exception of the main SF sites.
8. We also mapped other strong line ratios routinely used in the literature to map the ionisation structure, namely [O III]/[S II], [O III]/[O I], [O III]/[O II], and [S III]/[S II]. They closely follow the [O III]/Hβ map, with larger ratios at the main site of SF and decreasing outwards. We note that [O III]/[O II] in particular can reach values of up to ∼4.0, which is well in the range of the Lyman break galaxies at $z \sim 2-3$ and the Lyman continuum leakers.
9. We present maps for EW(Hα) and EW([O III]). Unsurprisingly, both present very high values that can reach up to ∼1500 Å at the Hα peak. The maps allowed us to delineate the ionised gas structure in the external part of the galaxy. In particular, we identified two structures roughly symmetric to the horns, with respect to the main body of the galaxy, that bend towards each other and form a close structure, called here 'the beard'.
10. The velocity fields of the strongest lines present an overall structure similar to the velocity field for atomic hydrogen with receding velocities in the east and approaching velocities in the west and south-west and a east-west velocity difference of $\Delta v \sim 40\,\mathrm{km\,s^{-1}}$. However, it is much more complex than simple rotation. The area between the horns presents a velocity stratification with redder velocities in the high ionisation lines and bluer velocities in the low ionisation lines. In addition, it is the only area in the galaxy with velocity dispersions clearly above the MUSE instrumental width.
11. The modelling of the stellar continuum suggests that most of the mass of the galaxy (∼60−70%) can be attributed to a relatively old ($\gtrsim$1 Gyr) stellar population. There is also a significant (∼10−30% in mass) contribution of an intermediate age (∼40−400 Myr) stellar population in the inner part of the galaxy. However, the luminosity of the galaxy is dominated by a young (i.e. ∼6 Myr) stellar population, even if it contributes only $\lesssim$10% to the stellar mass. The ages of these young stars in the selected apertures suggest that the most recent SF propagates from the outer to the inner parts of the galaxy, and most importantly from east to west. The Hα luminosity implies a total current SFR of $0.17\,M_\odot\,\mathrm{yr^{-1}}$.
12. We identified a point source presenting a local maximum in the [S II]/Hα and [O I]/Hα maps. We isolated the emission at the point source from the emission of the surrounding DIG. Given the upper limit for the physical size, its line ratios, and line widths ($\sigma \sim 50\,\mathrm{km\,s^{-1}}$), the most plausible point-like source causing this emission is a SNR.
13. We confirm the presence of WR stars in the galaxy by means of the red bump. Notably, the red bump emission does not peak at the same location as the maximum in Hα and where the most recent SF takes place, but towards the east, in what we named here H II-3. Given the suggested east-to-west SF propagation, we postulate the presence of WN stars at the maximum in Hα, which may be detected by deep and high spatial resolution observations of the blue bump.
14. We discuss the horns and the beard structures and posit that they represent two snapshots of the stellar feedback in action, more advance in the case of the horns, and at somewhat earlier stage for the beard. We suggest that the so-called horns represent the walls of a fragmented super-bubble that creates a passage where, perhaps, ionising photons from the youngest generation of stars could escape from the galaxy.

This ensemble of results exemplifies the potential of 2D detailed spectroscopic studies of dwarf star-forming galaxies at high spatial resolution to learn about the mechanisms at work in first galaxies, as well as to understand the biases inherent to similar studies on those actual galaxies, where such a level of detail, understood as the number of spectral features available as well as spatial resolution, is unattainable. JWST is already obtaining integrated spectra of primeval galaxies similar to the one studied here (Schaerer et al. 2022; Arellano-Córdova et al. 2022). In the not so distant future, thanks to its IFU mode, it will be able to map the physical and chemical properties of those same galaxies. Likewise, the cohort of extremely large telescopes will be equipped with IFS-based instruments in the near-infrared (i.e. HARMONI at the ELT Thatte et al. 2020; IRIS at the TMT Larkin et al. 2016; and GMTIFS at the GMT Sharp et al. 2016). This implies that in the not so distant future, we will be able to spectroscopically map the primeval galaxies at exquisite spatial resolution for which the present and similar works will undoubtedly constitute a key referent.

Acknowledgements. The authors want to thank Jorge Sánchez Almeida for discussions on different aspects of the work presented here. A.M.I. also thanks Begoña García-Lorenzo and acknowledges the Spanish Ministry of Science, Innovation and Universities (MCIU), and the Agencia Estatal de Investigación (project PID2019-107010GB-100) for the support during the initial phases of this project. P.M.W. gratefully acknowledges support by the BMBF through the ErUM programme (project VLT-BlueMUSE, grant 05A20BAB). Based on observations collected at the European Organisation for Astronomical Research in the Southern Hemisphere under ESO programme 0101.A-0282(A). We are also grateful to the communities who developed the many python packages used in this research, such MPDAF (Piqueras et al. 2017), Astropy (Astropy Collaboration 2013), numpy (Walt et al. 2011), scipy (Jones et al. 2001) and matplotlib (Hunter 2007).

References

Alloin, D., Collin-Souffrin, S., Joly, M., & Vigroux, L. 1979, A&A, 78, 200
Amorín, R., Aguerri, J. A. L., Muñoz-Tuñón, C., & Cairós, L. M. 2009, A&A, 501, 75
Amorín, R. O., Pérez-Montero, E., & Vílchez, J. M. 2010, ApJ, 715, L128
Amorín, R., Pérez-Montero, E., Vílchez, J. M., & Papaderos, P. 2012, ApJ, 749, 185
Ann, H. B., Seo, M., & Ha, D. K. 2015, ApJS, 217, 27
Annibali, F., & Tosi, M. 2022, Nat. Astron., 6, 48
Arellano-Córdova, K. Z., & Rodríguez, M. 2020, MNRAS, 497, 672
Arellano-Córdova, K. Z., Berg, D. A., Chisholm, J., et al. 2022, ApJ, 940, L23
Asplund, M., Amarsi, A. M., & Grevesse, N. 2021, A&A, 653, A141
Astropy Collaboration (Robitaille, T. P., et al.) 2013, A&A, 558, A33
Bacon, R., Accardo, M., Adjali, L., et al. 2010, Proc. SPIE, 7735, 773508

Baldwin, J. A., Phillips, M. M., & Terlevich, R. 1981, PASP, 93, 5
Benjamin, R. A., Skillman, E. D., & Smits, D. P. 1999, ApJ, 514, 307
Bergvall, N., Zackrisson, E., Andersson, B. G., et al. 2006, A&A, 448, 513
Bian, F., Kewley, L. J., & Dopita, M. A. 2018, ApJ, 859, 175
Bik, A., Östlin, G., Hayes, M., et al. 2015, A&A, 576, L13
Binette, L., Magris, C. G., Stasińska, G., & Bruzual, A. G. 1994, A&A, 292, 13
Bordalo, V., Plana, H., & Telles, E. 2009, ApJ, 696, 1668
Borthakur, S., Heckman, T. M., Leitherer, C., & Overzier, R. A. 2014, Science, 346, 216
Bosch, G., Hägele, G. F., Amorín, R., et al. 2019, MNRAS, 489, 1787
Bouwens, R. J., Illingworth, G. D., Oesch, P. A., et al. 2015, ApJ, 811, 140
Bouwens, R. J., Smit, R., Labbé, I., et al. 2016, ApJ, 831, 176
Brinchmann, J., Charlot, S., White, S. D. M., et al. 2004, MNRAS, 351, 1151
Brinchmann, J., Kunth, D., & Durret, F. 2008, A&A, 485, 657
Bruzual, G., & Charlot, S. 2003, MNRAS, 344, 1000
Cairós, L. M., Vílchez, J. M., González Pérez, J. N., Iglesias-Páramo, J., & Caon, N. 2001, ApJS, 133, 321
Cairós, L. M., González-Pérez, J. N., Weilbacher, P. M., & Manso Sainz, R. 2022, A&A, 664, A144
Cappellari, M. 2017, MNRAS, 466, 798
Cappellari, M., & Copin, Y. 2003, MNRAS, 342, 345
Cardamone, C., Schawinski, K., Sarzi, M., et al. 2009, MNRAS, 399, 1191
Cardelli, J. A., Clayton, G. C., & Mathis, J. S. 1989, ApJ, 345, 245
Cid Fernandes, R., Carvalho, M. S., Sánchez, S. F., de Amorim, A., & Ruschel-Dutra, D. 2021, MNRAS, 502, 1386
Crowther, P. A. 2007, ARA&A, 45, 177
Della Bruna, L., Adamo, A., Lee, J. C., et al. 2021, A&A, 650, A103
Dopita, M. A., Kewley, L. J., Sutherland, R. S., & Nicholls, D. C. 2016, Ap&SS, 361, 61
Duncan, K., & Conselice, C. J. 2015, MNRAS, 451, 2030
Eldridge, J. J., Izzard, R. G., & Tout, C. A. 2008, MNRAS, 384, 1109
Fernández, V., Amorín, R., Sanchez-Janssen, R., del Valle-Espinosa, M. G., & Papaderos, P. 2023, MNRAS, 520, 3576
Fesen, R. A., Blair, W. P., & Kirshner, R. P. 1985, ApJ, 292, 29
Flores-Fajardo, N., Morisset, C., Stasińska, G., & Binette, L. 2011, MNRAS, 415, 2182
Flury, S. R., Jaskot, A. E., Ferguson, H. C., et al. 2022a, ApJS, 260, 1
Flury, S. R., Jaskot, A. E., Ferguson, H. C., et al. 2022b, ApJ, 930, 126
García-Díaz, M. T., Henney, W. J., López, J. A., & Doi, T. 2008, Rev. Mex. Astron. Astrofis., 44, 181
García-Lorenzo, B., Cairós, L. M., Caon, N., Monreal-Ibero, A., & Kehrig, C. 2008, ApJ, 677, 201
Garnett, D. R. 1992, AJ, 103, 1330
Georgy, C., Ekström, S., Meynet, G., et al. 2012, A&A, 542, A29
Girardi, L., Bressan, A., Bertelli, G., & Chiosi, C. 2000, A&AS, 141, 371
Gomes, J. M., & Papaderos, P. 2017, A&A, 603, A63
González Delgado, R. M., Cerviño, M., Martins, L. P., Leitherer, C., & Hauschildt, P. H. 2005, MNRAS, 357, 945
Gunawardhana, M. L. P., Brinchmann, J., Weilbacher, P. M., et al. 2020, MNRAS, 497, 3860
Guseva, N. G., Izotov, Y. I., & Thuan, T. X. 2000, ApJ, 531, 776
Guseva, N. G., Izotov, Y. I., Papaderos, P., & Fricke, K. J. 2007, A&A, 464, 885
Hadfield, L. J., & Crowther, P. A. 2007, MNRAS, 381, 418
Heckman, T. M., Sembach, K. R., Meurer, G. R., et al. 2001, ApJ, 558, 56
Henkel, C., Hunt, L. K., & Izotov, Y. I. 2022, Galaxies, 10, 11
Herenz, E. C., Hayes, M., Papaderos, P., et al. 2017, A&A, 606, L11
Herenz, E. C., Inoue, J., Salas, H., et al. 2023, A&A, 670, A121
Hogarth, L., Amorín, R., Vílchez, J. M., et al. 2020, MNRAS, 494, 3541
Hunter, J. D. 2007, Comput. Sci. Eng., 9, 90
Izotov, Y. I., & Thuan, T. X. 1998, ApJ, 500, 188
Izotov, Y. I., Stasińska, G., Meynet, G., Guseva, N. G., & Thuan, T. X. 2006, A&A, 448, 955
Izotov, Y. I., Guseva, N. G., & Thuan, T. X. 2011, ApJ, 728, 161
Izotov, Y. I., Orlitová, I., Schaerer, D., et al. 2016, Nature, 529, 178
Izotov, Y. I., Worseck, G., Schaerer, D., et al. 2021, MNRAS, 503, 1734
James, B. L., Tsamis, Y. G., & Barlow, M. J. 2010, MNRAS, 401, 759
James, B. L., Tsamis, Y. G., Barlow, M. J., Walsh, J. R., & Westmoquette, M. S. 2013, MNRAS, 428, 86
Jones, E., Oliphant, T., Peterson, P., et al. 2001, SciPy: Open Source Scientific Tools for Python
Kehrig, C., Monreal-Ibero, A., Papaderos, P., et al. 2012, A&A, 540, A11
Kennicutt, R. C., & Evans, N. J. 2012, ARA&A, 50, 531
Kewley, L. J., & Ellison, S. L. 2008, ApJ, 681, 1183
Kewley, L. J., Dopita, M. A., Sutherland, R. S., Heisler, C. A., & Trevena, J. 2001, ApJ, 556, 121
Kopsacheili, M., Zezas, A., & Leonidaki, I. 2020, MNRAS, 491, 889
Kreckel, K., Groves, B., Bigiel, F., et al. 2017, ApJ, 834, 174
Kreckel, K., Egorov, O. V., Belfiore, F., et al. 2022, A&A, 667, A16
Krumholz, M. R., Adamo, A., Fumagalli, M., et al. 2015, ApJ, 812, 147
Kumari, N., James, B. L., & Irwin, M. J. 2017, MNRAS, 470, 4618
Kumari, N., James, B. L., Irwin, M. J., Amorín, R., & Pérez-Montero, E. 2018, MNRAS, 476, 3793
Kunth, D., & Östlin, G. 2000, A&ARv, 10, 1
Larkin, J. E., Moore, A. M., Wright, S. A., et al. 2016, in Ground-based and Airborne Instrumentation for Astronomy VI, eds. C. J. Evans, L. Simard, & H. Takami, SPIE Conf. Ser., 9908, 99081W
Leitherer, C., Schaerer, D., Goldader, J. D., et al. 1999, ApJS, 123, 3
Lindegren, L., Hernández, J., Bombrun, A., et al. 2018, A&A, 616, A2
Lintott, C. J., Schawinski, K., Slosar, A., et al. 2008, MNRAS, 389, 1179
Liu, X.-W., Storey, P. J., Barlow, M. J., et al. 2000, MNRAS, 312, 585
Lofthouse, E. K., Houghton, R. C. W., & Kaviraj, S. 2017, MNRAS, 471, 2311
López-Sánchez, Á. R., Esteban, C., García-Rojas, J., Peimbert, M., & Rodríguez, M. 2007, ApJ, 656, 168
López-Sánchez, Á. R., & Esteban, C. 2010, A&A, 516, A104
Luridiana, V., Morisset, C., & Shaw, R. A. 2015, A&A, 573, A42
Marino, R. A., Rosales-Ortega, F. F., Sánchez, S. F., et al. 2013, A&A, 559, A114
Mathewson, D. S., & Clarke, J. N. 1973, ApJ, 180, 725
Menacho, V., Östlin, G., Bik, A., et al. 2021, MNRAS, 506, 1777
Meynet, G., & Maeder, A. 2005, A&A, 429, 581
Mezcua, M., Lobanov, A. P., Mediavilla, E., & Karouzos, M. 2014, ApJ, 784, 16
Micheva, G., Östlin, G., Zackrisson, E., et al. 2013, A&A, 556, A10
Micheva, G., Oey, M. S., Jaskot, A. E., & James, B. L. 2017, ApJ, 845, 165
Micheva, G., Christian Herenz, E., Roth, M. M., Östlin, G., & Girichidis, P. 2019, A&A, 623, A145
Moffat, A. F. J. 1969, A&A, 3, 455
Monreal-Ibero, A., & Walsh, J. R. 2020a, A&A, 634, A47
Monreal-Ibero, A., & Walsh, J. R. 2020b, VizieR Online Data Catalog: J/A+A/634/A47
Monreal-Ibero, A., Arribas, S., & Colina, L. 2006, ApJ, 637, 138
Monreal-Ibero, A., Colina, L., Arribas, S., & García-Marín, M. 2007, A&A, 472, 421
Monreal-Ibero, A., Vílchez, J. M., Walsh, J. R., & Muñoz-Tuñón, C. 2010a, A&A, 517, A27
Monreal-Ibero, A., Arribas, S., Colina, L., et al. 2010b, A&A, 517, A28
Monreal-Ibero, A., Relaño, M., Kehrig, C., et al. 2011, MNRAS, 413, 2242
Monreal-Ibero, A., Walsh, J. R., & Vílchez, J. M. 2012, A&A, 544, A60
Monreal-Ibero, A., Walsh, J. R., Westmoquette, M. S., & Vílchez, J. M. 2013, A&A, 553, A57
Monreal-Ibero, A., Walsh, J. R., Iglesias-Páramo, J., et al. 2017, A&A, 603, A130
Monreal-Ibero, A., Weilbacher, P. M., & Wendt, M. 2018, A&A, 615, A33
Morales-Luis, A. B., Pérez-Montero, E., Sánchez Almeida, J., & Muñoz-Tuñón, C. 2014, ApJ, 797, 81
Moustakas, J., & Kennicutt, R. C., Jr. 2006, ApJS, 164, 81
Nakajima, K., & Ouchi, M. 2014, MNRAS, 442, 900
Nicholls, D. C., Dopita, M. A., Sutherland, R. S., et al. 2014, ApJ, 786, 155
Osterbrock, D. E., & Ferland, G. J. 2006, Astrophysics of Gaseous Nebulae and Active Galactic Nuclei (Sausalito, CA: University Science Books)
Paalvast, M., & Brinchmann, J. 2017, MNRAS, 470, 1612
Papaderos, P., Gomes, J. M., Vílchez, J. M., et al. 2013, A&A, 555, L1
Paudel, S., Smith, R., Yoon, S. J., Calderón-Castillo, P., & Duc, P.-A. 2018, ApJS, 237, 36
Payne, J. L., White, G. L., Filipović, M. D., & Pannuti, T. G. 2007, MNRAS, 376, 1793
Payne, J. L., White, G. L., & Filipović, M. D. 2008, MNRAS, 383, 1175
Pellegrini, E. W., Oey, M. S., Winkler, P. F., et al. 2012, ApJ, 755, 40
Pérez-Montero, E., Amorín, R., Sánchez Almeida, J., et al. 2021, MNRAS, 504, 1237
Pilyugin, L. S., & Grebel, E. K. 2016, MNRAS, 457, 3678
Piqueras, L., Conseil, S., Shepherd, M., et al. 2017, ArXiv e-prints [arXiv:1710.03554]
Porter, R. L., Ferland, G. J., Storey, P. J., & Detisch, M. J. 2013, MNRAS, 433, L89
Poznanski, D., Prochaska, J. X., & Bloom, J. S. 2012, MNRAS, 426, 1465
Ramambason, L., Schaerer, D., Stasińska, G., et al. 2020, A&A, 644, A21
Roth, M. M., Sandin, C., Kamann, S., et al. 2018, A&A, 618, A3
Roth, M. M., Jacoby, G. H., Ciardullo, R., et al. 2021, ApJ, 916, 21
Sánchez Almeida, J., Elmegreen, B. G., Muñoz-Tuñón, C., & Elmegreen, D. M. 2014, A&ARv, 22, 71
Schaerer, D., Marques-Chaves, R., Barrufet, L., et al. 2022, A&A, 665, L4
Schlafly, E. F., & Finkbeiner, D. P. 2011, ApJ, 737, 103
Sharp, R., Bloxham, G., Boz, R., et al. 2016, in Ground-based and Airborne Instrumentation for Astronomy VI, eds. C. J. Evans, L. Simard, & H. Takami, SPIE Conf. Ser., 9908, 99081Y

Stasińska, G. 2006, A&A, 454, L127
Storchi-Bergmann, T., Calzetti, D., & Kinney, A. L. 1994, ApJ, 429, 572
Telles, E., & Terlevich, R. 1995, MNRAS, 275, 1
Telles, E., Thuan, T. X., Izotov, Y. I., & Carrasco, E. R. 2014, A&A, 561, A64
Thatte, N. A., Bryson, I., Clarke, F., et al. 2020, SPIE Conf. Ser., 11447, 114471W
Thuan, T. X., & Martin, G. E. 1981, ApJ, 247, 823
Torres-Peimbert, S., & Peimbert, M. 1977, Rev. Mex. Astron. Astrofis., 2, 181
Tumlinson, J., Peeples, M. S., & Werk, J. K. 2017, ARA&A, 55, 389
van Zee, L., Skillman, E. D., & Salzer, J. J. 1998, AJ, 116, 1186
Veilleux, S., & Osterbrock, D. E. 1987, ApJS, 63, 295
Vriend, W. J. 2015, Science Operations 2015: Science Data Management – An ESO/ESA Workshop, 1
Walt, S. V. D., Colbert, S. C., & Varoquaux, G. 2011, Comput. Sci. Eng., 13, 22
Weilbacher, P. M., Duc, P. A., & Fritze-v. Alvensleben, U. 2003, A&A, 397, 545
Weilbacher, P. M., Monreal-Ibero, A., Kollatschny, W., et al. 2015, A&A, 582, A114
Weilbacher, P. M., Monreal-Ibero, A., Verhamme, A., et al. 2018, A&A, 611, A95
Weilbacher, P. M., Palsa, R., Streicher, O., et al. 2020, A&A, 641, A28
Westmoquette, M. S., James, B., Monreal-Ibero, A., & Walsh, J. R. 2013, A&A, 550, A88
Xiao, L., Stanway, E. R., & Eldridge, J. J. 2018, MNRAS, 477, 904
Zhang, Y., Liu, X.-W., Liu, Y., & Rubin, R. H. 2005, MNRAS, 358, 457
Zhang, K., Yan, R., Bundy, K., et al. 2017, MNRAS, 466, 3217